12-2020

An Investigation Into The Effects Of Aluminum Substitution And Aging Under Aerobic Conditions On The Physicochemical Properties Of Ferrihydrite

Sean Zigah

AN INVESTIGATION INTO THE EFFECTS OF ALUMINUM SUBSTITUTION AND AGING UNDER AEROBIC CONDITIONS ON THE PHYSICOCHEMICAL PROPERTIES OF FERRIHYDRITE

by

SEAN CHRISTOPHER ZIGAH

Under the Direction of Dr. Nadine Kabengi, PhD

ABSTRACT

This thesis characterizes the physicochemical properties of pure (Fh) and aluminum-doped ferrihydrites (AlFh) upon aging and puts forth a hypothesis involving the lattice position occupied by Al within Fh. We used flow and drop solution microcalorimetry, X-ray diffraction, adsorption spectroscopy and magnetic circular dichroism spectroscopy to carry a complete characterization. Aging of pure Fh showed evidence for phase transformation into varying amounts of hematite (Ht) and goethite (Gt) with the former increasing over time. The presence of Al retarded all transformation. Aged AlFhs showed a larger heat of exchange (Q_{exch}) compared to undoped Fhs and increased with age. Results also showed increased magnetism, contraction of the lattice c-axis, heats of phosphate adsorption, and pH decrease with Al incorporation. We posit that Al substitution occurs on the surface of Fh in an octahedrally-coordinated Fe site.

INDEX WORDS: Ferrihydrite, Aging, Aluminum substitution, Microcalorimetry, Total scattering

AN INVESTIGATION INTO THE EFFECTS OF ALUMINUM SUBSTITUTION AND AGING UNDER AEROBIC CONDITIONS ON THE PHYSICOCHEMICAL PROPERTIES OF FERRIHYDRITE

by

SEAN CHRISTOPHER ZIGAH

A Thesis Submitted in Partial Fulfillment of the Requirements for the Degree of

Masters of Science

in the College of Arts and Sciences

Georgia State University

2020

AN INVESTIGATION INTO THE EFFECTS OF ALUMINUM SUBSTITUTION AND AGING UNDER AEROBIC CONDITIONS ON THE PHYSICOCHEMICAL PROPERTIES OF FERRIHYDRITE

by

SEAN CHRISTOPHER ZIGAH

Committee Chair: Nadine Kabengi

Committee: Marc Michel

Michael Machesky

Daniel Deocampo

Electronic Version Approved:

Office of Graduate Services

College of Arts and Sciences

Georgia State University

August 2020

DEDICATION

To Jennifer Grant

ACKNOWLEDGEMENTS

I would like to thank everyone in my life up until this point, but I would like to acknowledge a few people in particular. Without my parents and my siblings, I would not even know where to begin, and I am eternally grateful for their remote yet constant support in helping me get to this point. I would like to acknowledge the Herculean efforts by my partner Summer, for helping me to stay the course and find another gear even when I felt exhausted. I would like to acknowledge my mentor Dr. Nadine Kabengi, without whom none of this text exists and her insight and personal contributions to this thesis and to my life as a whole cannot be understated and for her efforts, I am forever indebted. Lastly, I would like to say thanks to Faisal Adams; a soon-to-be lifelong friend without whom I surely would have fizzled out and moved back to my old house in Tema. Faisal's contributions to this work and the person I am are immeasurable so to put it simply, thank you.

TABLE OF CONTENTS

LIST OF TABLES

LIST OF FIGURES

LIST OF ABBREVIATIONS

FMC	Flow Adsorption Microcalorimetry
ΔHads	Enthalpy of Adsorption
BET	Brunauer–Emmett–Teller
Qexch	Heat of Exchange
PDF	X-ray Pair Distribution Function analysis
Al	Aluminum
Fh	Ferrihydrite
Gt	Goethite
Ht	Hematite
Gb	Gibbsite
XRD	X-ray Diffraction
[C/N]	Reaction of Nitrate Replacing Chloride
[N/C]	Reaction of Chloride Replacing Nitrate
EXAFS	X-ray Absorption Fine Structure
XAS	X-ray Absorption
XMCD	X-ray Magnetic Circular Dichroism
SSA	Specific Surface Area
AlFh	Aluminum Ferrihydrite
Q_{exch}	Heat of Exchange
K_s	Equilibrium Constant

1 INTRODUCTION

Ferrihydrite (Fh, $Fe_5O_8OH.4H_2O$) is an environmentally prevalent nanocrystalline iron oxyhydroxide mineral that plays an essential part in a host of geochemical processes, namely the biogeochemical cycling of iron and the transport of natural and anthropogenic contaminants in aqueous and terrestrial systems (Jambor and Dutrizac 1998, Cornell and Schwertmann 2003, Masue et al., 2007). In aquatic environments, the presence of Fh has been shown to increase methane emission by approximately 26.4% (Yan and Zhou 2019). Fh has been detected in Martian soil and is present on several meteorites (Tomeoka and Buseck 1988, Bishop et al., 1992, Weitz and Bishop 2019). In addition to its importance in geologic systems, Fh is a precursor phase in several materials that have technological and catalytic applications (Cornell and Schwertmann 2003). Finally, due to its resemblance to the nanocrystalline form of ferritin, an iron-storing protein, Fh, and its structure are relevant to biological applications (Michel et al., 2010). Fh possesses high surface reactivity owing to its very high specific surface areas for which values as high as 1250 m^2/g have been reported (Villalobos and Antelo 2011). Compared to other iron oxide minerals, Fh is thermodynamically metastable and over time, undergoes phase transformations to more stable crystalline iron oxide minerals such as hematite (Ht) and goethite (Gt) (Majzlan et al., 2004, Zhang et al., 2018). These phase transformations depend on a host of physicochemical factors, most notably aging time, temperature, pH, and presence or absence of oxygen during synthesis and storage, etc. (Schwertmann and Murad 1983, Kukkadapu et al., 2003, Cudennec and Lecerf 2006, Hu et al., 2014). Given Fh's ubiquitousness, high reactivity, and inherent variability in structure and transformations under different environmental conditions, there is a clear need to understand how these factors, alone and in tandem, affect Fh properties.

1.1 Structure of Ferrihydrite

The current state of the literature regarding models for the structure of Fh highlights the difficulty in characterizing this nanocrystalline mineral. Over the past few decades, different and contradicting models have attempted to represent the structure of Fh (Eggleton and Fitzpatrick 1988, Drits et al., 1993, Michel et al., 2007, Maillot et al., 2011). Currently, albeit not without debate (Manceau et al., 2014), the most widely used structural model for Fh is the Michel model, which was formulated based on results from X-ray pair-distribution function analysis (PDF) (Michel et al., 2007). Michel's model expresses Fh as a single-crystalline phase comparable to the iron (Fe) equivalent of $Al_{10}O_{14}(OH)_2$ (akdalaite), with an isostructural motif similar to that of a Keggin moiety. Within the structure, Fe atoms occupy three types of positions denoted as Fe_1, Fe_2, and Fe_3; Fe_1 and Fe_2 atoms are octahedrally coordinated to central Fe_3 atoms that are in tetrahedral coordination (Figure 1-1). Based on this model, Fh is composed of roughly 80% Fe in octahedral coordination and 20% Fe in tetrahedral coordination (Michel et al., 2007). The reactivity of Fh is thought to be strongly associated with the singly coordinated (-OH) groups associated with the Fe_1 octahedra (Hiemstra 2013). According to the quantitative surface depletion model for Fh, which was developed to describe the surface structure of Fh, Fe_1 octahedra stick out from crystallographic faces, particularly the 1-10 and 1-11 faces that contribute over 75% of the total surface area. The resulting structure is depleted on the surface with respect to Fe_2 and Fe_3 (Hiemstra 2013).

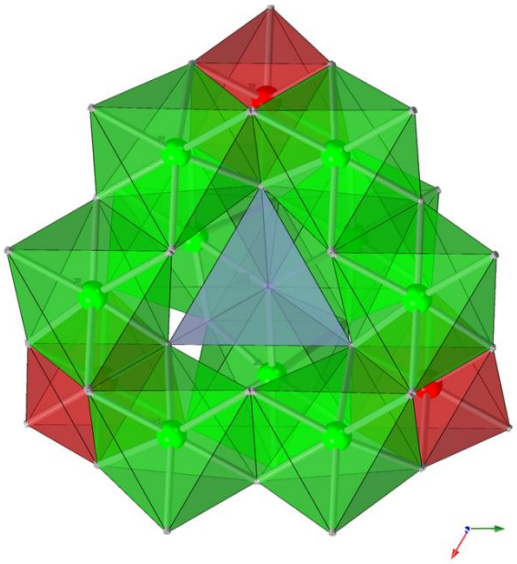

Figure 1-1: Fh Keggin cluster showing the different lattice positions for Fe: Fe_1 (in green), Fe_2 (in red), and Fe_3 polyhedra (in blue).

Michel's model has come under scrutiny from Manceau et al. (2014), who argued that the parameters used to constrain the model are oversimplified and insufficient. Specifically, the authors point to the omission of structural defects or inhomogeneities, and the lack of evidence from previously-conducted extended X-ray absorption fine structure (EXAFS) studies to suggest the presence of tetrahedrally-coordinated Fe (Maillot et al., 2011, Peak and Regier 2012, Manceau et al., 2014). However, a recent study (Funnell et al., 2020) showed, using a nanocomposite reverse Monte Carlo approach, that the Michel model was in better agreement with X-ray total scattering results, and was, therefore, a better representation of the short to intermediate-ranged nature of Fh then the model put forth by Drits et al. (1993). The Drits model does not contain tetrahedral Fe and describes a system consisting of a mixture of defective and defect-free Fh with "ultradispersed hematite". There is no clear consensus in the literature regarding the validity of the two models as the debate is still ongoing (Manceau 2019, Sassi and Rosso 2019).

1.2 Phase Transformation of Ferrihydrite

Fh ($K_s = 10^{-39}$) is relatively metastable compared to hematite (Ht; α-Fe_2O_3; $K_s = 10^{-43}$) and goethite (Gt; α-FeOOH; $K_s = 10^{-41}$) and, at room temperature, will directly transform over time into either mineral, although Gt has been seen as an intermediate phase during Fh crystallization into Ht (Jambor and Dutrizac 1998, Majzlan et al., 2004, Hansel et al., 2005, Das et al., 2011, Zhang et al., 2018). The transformation of Fh to Ht follows a solid-state mechanism involving the release of structural water from Fh and reassembly of the lattice constituents (Schwertmann and Murad 1983), while that of Fh to Gt occurs via dissolution and reprecipitation (Schwertmann and Murad 1983, Cornell and Schwertmann 2003). Ht forms at relatively neutral pH conditions (approx. 7-9), whereas Gt forms at predominantly at pH values of 4 and 11 (Cornell and Schwertmann 2003). The transformation of Fh into other more thermodynamically-stable iron oxides depends on a multitude of factors, such as the duration of aging, pH conditions, temperature, and the presence of impurities (Schwertmann and Murad 1983, Dzombak and Morel 1990, Jambor and Dutrizac 1998, Cornell and Schwertmann 2003, Kukkadapu et al., 2003, Cismasu et al., 2011, Das et al., 2011, Hu et al., 2014).

1.3 Aluminum Substitution in Fh

Previous studies have investigated the effects of impurities, particularly aluminum (Al), on Fh's structure, composition, chemical reactivity, and mineralization pathways (Cismasu et al., 2012, Cismasu et al., 2013, Manceau and Gates 2013, Hu et al., 2014, Johnston and Chrysochoou 2016, Namayandeh and Kabengi 2019). Al is a noteworthy impurity and substituent into Fh (AlFh) because of its prevalence and availability within natural systems as well as its capacity to isostructurally substitute for Fe^{3+} due to slightly smaller atomic size and charge. Cismasu et al. (2012) have shown that 20-30 mol% Al concentration is the potential upper limit of substitution

into the structure of Fh, with a distinct gibbsite phase (Gb; $Al(OH)_3$) forming at Al concentrations above 30 mol% Al. Manceau et al. (2014) further refined the Al-substitution upper limit to ~ 24%, suggesting that this constraint results from Al-Al avoidance within the AlFh structure as the adjacent polyhedra configuration would be energetically unfavorable. The detection of Gb formation in Fh samples bearing Al in concentrations greater than 25 mol% (Schwertmann et al., 1979) aligns well with the explanation offered by Manceau et al. (2014).

The lattice position that Al occupies, assuming isostructural substitution into Fh, is still unclear and is challenging to assess due to the limitations of current macroscopic and spectroscopic techniques. Using K-edge X-ray absorption near edge structure (XANES), Cismasu et al. (2012) found Al atoms within several Al-doped Fh (AlFh) samples predominantly in octahedral coordination, thus potentially substituting either an octahedral Fe_1 or Fe_2 site, i.e., eliminating the tetrahedral coordinated Fe_3 position as a contender for a substitution site. Furthermore, results from computational work using density functional theory (DFT) calculations on Al-bearing Fhs showed an energetic preference for Al to occupy the Fe_1 lattice position relative to the Fe_2 and Fe_3 sites in Michel's single-phase structure model (Kubicki et al., 2012)

Metal cation substitution, such as Al, has been shown to suppress the phase transformation rate of Fh into either Gt or Ht (Cornell et al., 1987, Schwertmann et al., 2000, Jentzsch and Penn 2006, Hansel et al., 2011), and affect the interactions of ions and ligands such as phosphorus, arsenic, selenate, chromate, zinc, and lead with the surface, although it is not always clear in which direction (Trivedi et al., 2003, Hansel et al., 2011, Liu and Hesterberg 2011, Adra et al., 2013, Cismasu et al., 2013, Johnston and Chrysochoou 2016, Gypser et al., 2018, Namayandeh and Kabengi 2019). A recent study on sulfate adsorption on Al-bearing Fh by Namayandeh and Kabengi (2019) showed an increase in the heat of adsorption and in the inner-sphere complexation

fraction with increasing Al content. This contradicts findings from Johnston and Chrysochoou (2016), who showed an increase in the outer-sphere fraction of selenate, chromate, and sulfate with increasing Al.

1.4 Overview

The goal of this work is two-fold: first, to assess the effect of Al doping and aging duration on the transformations of AlFh, and second to test the hypothesis that, assuming isostructural substitution of Fe by Al, Al occupies the Fe_1 lattice position on the surface. Chapter 2 consists of a detailed physicochemical characterization of Fh and AlFh samples that had been aging at room temperature and under aerobic conditions for various time durations. The conditions were chosen to mimic environmental variables. The characterization of AlFh samples with different mol% Al showcases data detailing their crystallinity and phases composition with aging, their magnetic properties, and atomic coordination geometries, specific surface areas, surface energies, as well as surface charge properties and reactivity. In Chapter 3, the lattice position of Al within Fh's structure is investigated by testing a hypothesis formulated based on results from previous spectroscopic and thermodynamic studies. We hypothesize that Al atoms are substituting for Fe atoms occupying the singly coordinated Fe_1 octahedra, which dominates the Fh nanoparticle surface and is directly associated with Fh reactivity. Characterizing and assessing the influence of Al doping, particularly considering its prevalence in natural systems, is imperative to understanding modeling and predicting Fh behavior under a broader range of complex and more realistic environmental conditions.

REFERENCES

Adra, A., G. Morin, G. Ona-Nguema, N. Menguy, F. Maillot, C. Casiot, O. Bruneel, S. Lebrun, F. Juillot and J. Brest (2013). "Arsenic scavenging by aluminum-substituted ferrihydrites in a circumneutral pH river impacted by acid mine drainage." Environ Sci Technol **47**(22): 12784-12792.

Bishop, J., C. Pieters and R. Burns (1992). Ferrihydrite found in Fe-rich montmorillonite and its relationship to the reflectance spectra of Mars. Lunar and Planetary Science Conference.

Cismasu, A. C., C. Levard, F. M. Michel and G. E. Brown (2013). "Properties of impurity-bearing ferrihydrite II: Insights into the surface structure and composition of pure, Al- and Si-bearing ferrihydrite from Zn(II) sorption experiments and Zn K-edge X-ray absorption spectroscopy." Geochimica et Cosmochimica Acta **119**: 46-60.

Cismasu, A. C., F. M. Michel, J. F. Stebbins, C. Levard and G. E. Brown (2012). "Properties of impurity-bearing ferrihydrite I. Effects of Al content and precipitation rate on the structure of 2-line ferrihydrite." Geochimica et Cosmochimica Acta **92**: 275-291.

Cismasu, A. C., F. M. Michel, A. P. Tcaciuc, T. Tyliszczak and J. G. E. Brown (2011). "Composition and structural aspects of naturally occurring ferrihydrite." Comptes Rendus Geoscience **343**(2-3): 210-218.

Cornell, R., R. Giovanoli and P. Schindler (1987). "Effect of silicate species on the transformation of ferrihydrite into goethite and hematite in alkaline media." Clays and Clay Minerals **35**(1): 21-28.

Cornell, R. M. and U. Schwertmann (2003). The iron oxides: structure, properties, reactions, occurrences and uses, John Wiley & Sons.

Cudennec, Y. and A. Lecerf (2006). "The transformation of ferrihydrite into goethite or hematite, revisited." Journal of Solid State Chemistry **179**(3): 716-722.

Das, S., M. J. Hendry and J. Essilfie-Dughan (2011). "Transformation of Two-Line Ferrihydrite to Goethite and Hematite as a Function of pH and Temperature." Environmental Science & Technology **45**(1): 268-275.

Drits, V., B. Sakharov, A. Salyn and A. Manceau (1993). "Structural model for ferrihydrite." Clay Minerals **28**(2): 185-207.

Dzombak, D. A. and F. M. Morel (1990). Surface complexation modeling: hydrous ferric oxide, John Wiley & Sons.

Eggleton, R. A. and R. W. Fitzpatrick (1988). "New data and a revised structural model for ferrihydrite." Clays and Clay minerals **36**(2): 111-124.

Funnell, N. P., M. F. Fulford, S. Inoué, K. Kletetschka, F. M. Michel and A. L. J. C. C. Goodwin (2020). "Nanocomposite structure of two-line ferrihydrite powder from total scattering." **3**(1): 1-9.

Gypser, S., F. Hirsch, A. M. Schleicher and D. Freese (2018). "Impact of crystalline and amorphous iron-and aluminum hydroxides on mechanisms of phosphate adsorption and desorption." Journal of Environmental Sciences **70**: 175-189.

Hansel, C. M., S. G. Benner and S. Fendorf (2005). "Competing Fe (II)-induced mineralization pathways of ferrihydrite." Environmental Science & Technology **39**(18): 7147-7153.

Hansel, C. M., D. R. Learman, C. J. Lentini and E. B. Ekstrom (2011). "Effect of adsorbed and substituted Al on Fe(II)-induced mineralization pathways of ferrihydrite." Geochimica et Cosmochimica Acta **75**(16): 4653-4666.

Hiemstra, T. (2013). "Surface and mineral structure of ferrihydrite." Geochimica et Cosmochimica Acta **105**: 316-325.

Hu, Y., Q. Li, B. Lee and Y. S. Jun (2014). "Aluminum affects heterogeneous Fe(III) (Hydr)oxide nucleation, growth, and ostwald ripening." Environ Sci Technol **48**(1): 299-306.

Jambor, J. L. and J. E. Dutrizac (1998). "Occurrence and Constitution of Natural and Synthetic Ferrihydrite, a Widespread Iron Oxyhydroxide." Chemical Reviews **98**(7): 2549-2586.

Jentzsch, T. L. and R. L. Penn (2006). "Influence of Aluminum Doping on Ferrihydrite Nanoparticle Reactivity." The Journal of Physical Chemistry B **110**(24): 11746-11750.

Johnston, C. P. and M. Chrysochoou (2016). "Mechanisms of Chromate, Selenate, and Sulfate Adsorption on Al-Substituted Ferrihydrite: Implications for Ferrihydrite Surface Structure and Reactivity." Environ Sci Technol **50**(7): 3589-3596.

Kubicki, J. D., M. Aryanpour, L. Kabalan and Q. Zhu (2012). "Quantum mechanical calculations on FeOH nanoparticles." Geoderma **189-190**: 236-242.

Kukkadapu, R. K., J. M. Zachara, J. K. Fredrickson, S. C. Smith, A. C. Dohnalkova and C. K. Russell (2003). "Transformation of 2-line ferrihydrite to 6-line ferrihydrite under oxic and anoxic conditions." American Mineralogist **88**(11-12): 1903-1914.

Liu, Y. T. and D. Hesterberg (2011). "Phosphate bonding on noncrystalline Al/Fe-hydroxide coprecipitates." Environ Sci Technol **45**(15): 6283-6289.

Maillot, F., G. Morin, Y. Wang, D. Bonnin, P. Ildefonse, C. Chaneac and G. Calas (2011). "New insight into the structure of nanocrystalline ferrihydrite: EXAFS evidence for tetrahedrally coordinated iron(III)." Geochimica et Cosmochimica Acta **75**(10): 2708-2720.

Majzlan, J., A. Navrotsky and U. Schwertmann (2004). "Thermodynamics of iron oxides: Part III. Enthalpies of formation and stability of ferrihydrite (∼Fe(OH)3), schwertmannite (∼FeO(OH)3/4(SO4)1/8), and ε-Fe2O3 1 1Associate editor: D. Wesolowski." Geochimica et Cosmochimica Acta **68**(5): 1049-1059.

Manceau, A. (2019). "Comment on “Roles of Hydration and Magnetism on the Structure of Ferrihydrite from First Principles”." ACS Earth and Space Chemistry **3**(8): 1576-1580.

Manceau, A. and W. P. Gates (2013). "Incorporation of Al in iron oxyhydroxides: implications for the structure of ferrihydrite." Clay Minerals **48**(3): 481-489.

Manceau, A., S. Skanthakumar and L. Soderholm (2014). "PDF analysis of ferrihydrite: Critical assessment of the under-constrained akdalaite model." American Mineralogist **99**(1): 102-108.

Masue, Y., R. H. Loeppert and T. A. Kramer (2007). "Arsenate and Arsenite Adsorption and Desorption Behavior on Coprecipitated Aluminum:Iron Hydroxides." Environmental Science & Technology **41**(3): 837-842.

Michel, F. M., L. Ehm, S. M. Antao, P. L. Lee, P. J. Chupas, G. Liu, D. R. Strongin, M. A. A. Schoonen, B. L. Phillips and J. B. Parise (2007). "The Structure of Ferrihydrite, a Nanocrystalline Material." Science **316**(5832): 1726-1729.

Michel, F. M., H.-A. Hosein, D. B. Hausner, S. Debnath, J. B. Parise and D. R. Strongin (2010). "Reactivity of ferritin and the structure of ferritin-derived ferrihydrite." Biochimica et Biophysica Acta (BBA)-General Subjects **1800**(8): 871-885.

Namayandeh, A. and N. Kabengi (2019). "Calorimetric study of the influence of aluminum substitution in ferrihydrite on sulfate adsorption and reversibility." J Colloid Interface Sci **540**: 20-29.

Peak, D. and T. Regier (2012). "Direct observation of tetrahedrally coordinated Fe(III) in ferrihydrite." Environ Sci Technol **46**(6): 3163-3168.

Sassi, M. and K. M. Rosso (2019). "Reply to “Comment on ‘Roles of Hydration and Magnetism on the Structure of Ferrihydrite from First Principles’”." ACS Earth and Space Chemistry **3**(8): 1581-1583.

Schwertmann, U., R. Fitzpatrick, R. Taylor and D. Lewis (1979). "The influence of aluminum on iron oxides. Part II. Preparation and properties of Al-substituted hematites." Clays and Clay Minerals **27**(2): 105-112.

Schwertmann, U., J. Friedl, H. Stanjek and D. G. Schulze (2000). "The effect of Al on Fe oxides. XIX. Formation of Al-substituted hematite from ferrihydrite at 25 C and pH 4 to 7." Clays and Clay Minerals **48**(2): 159-172.

Schwertmann, U. and E. Murad (1983). "Effect of pH on the formation of goethite and hematite from ferrihydrite." Clays and Clay Minerals **31**(4): 277-284.

Tomeoka, K. and P. R. Buseck (1988). "Matrix mineralogy of the Orgueil CI carbonaceous chondrite." Geochimica et Cosmochimica Acta **52**(6): 1627-1640.

Trivedi, P., J. A. Dyer and D. L. Sparks (2003). "Lead sorption onto ferrihydrite. 1. A macroscopic and spectroscopic assessment." Environmental science & technology **37**(5): 908-914.

Villalobos, M. and J. J. R. i. d. c. a. Antelo (2011). "A unified surface structural model for ferrihydrite: Proton charge, electrolyte binding, and arsenate adsorption." **27**(2): 139-151.

Weitz, C. M. and J. L. Bishop (2019). "Formation of clays, ferrihydrite, and possible salts in Hydrae Chasma, Mars." Icarus **319**: 392-406.

Yan, W. and Y. J. S. o. t. t. e. Zhou (2019). "The presence of ferrihydrite enhances greenhouse gas-methane emission in the environment." **688**: 462-469.

Zhang, D., S. Wang, Y. Wang, M. A. Gomez, Y. Duan and Y. Jia (2018). "The Transformation of Two-Line Ferrihydrite into Crystalline Products: Effect of pH and Media (Sulfate versus Nitrate)." ACS Earth and Space Chemistry **2**(6): 577-587.

2 PROPERTIES AND TRANSFORMATION PATHWAYS OF FH UNDER AEROBIC CONDITIONS

2.1 Introduction

Ferrihydrite (Fh; $Fe_5HO_8.4H_2O$) is an environmentally prevalent nano-crystalline mineral that plays an essential role in the biogeochemical cycling of iron and the transport of natural and anthropogenic contaminants in aqueous and terrestrial systems (Jambor and Dutrizac 1998, Cornell and Schwertmann 2003, Masue et al., 2007). Owing to its metastability, Fh slowly transforms at room temperature into more crystalline ferric iron, Fe(III), polymorphs namely either hematite (Ht, α-Fe_2O_3, $K_s = 10^{-43}$) or goethite (Gt, α-FeOOH, $K_s = 10^{-41}$) (Schwertmann and Murad 1983, Jambor and Dutrizac 1998, Majzlan et al., 2004, Hansel et al., 2005, Zhang et al., 2018).

The evolution of Fh into either Ht or Gt occurs predominantly via two mechanisms; Ht forms via the release of structural water (internal dehydration) and a rearrangement of the lattice structure whereas Gt forms directly through a dissolution process, causing a release of Fe(III) ions, which then preferentially orient to aggregate and reprecipitate (Schwertmann and Murad 1983, Burleson and Penn 2006). Gt serves as an intermediate phase during Fh crystallization into Ht (Das et al., 2011). The transformation pathways of Fh are influenced by a myriad of factors, such as aging duration, temperature, and solution chemistries. At near neutral pH values (~ 7-9), Ht is the favored transformation product, whereas, maximum Gt formation occurs at both very acidic and alkaline pH values that maximize the activity of $Fe(OH)^{2+}$ and $Fe(OH)_4^-$ species (pH values of 4 and 12) (Schwertmann and Murad 1983, Cornell and Schwertmann 2003, Burleson and Penn 2006, Cudennec and Lecerf 2006).

In natural environments, Fh seldom exists as a “pure” phase instead occurring with several dopants and substituents for Fe(III), notably aluminum (Al), whose incorporation is facilitated by

its abundance in natural systems and similarity in both charge and size to Fe(III) (Jambor and Dutrizac 1998, Cornell and Schwertmann 2003). Studies have shown that 20-30 mol% is the upper limit of isostructural Al substitution in Fh, with a distinct gibbsite phase forming at Al concentrations between 20-30 mol% (Cismasu et al., 2012). Manceau et al. (2013) proposed that due to Al-Al avoidance within the structure of Al-bearing Fh (AlFh), the maximum Al concentration that could be substituted into Fh is, in fact, lower at approximately 24 mol%. Their report is consistent with previous work, which found that gibbsite formation was detectable at Al concentrations greater than 25 mol% (Schwertmann et al., 1979).

Several studies have investigated the impact of Al doping on the structure, composition, and chemical reactivity of Fh and other iron oxides (Ekstrom et al., 2010, Bazilevskaya et al., 2011, Hansel et al., 2011, Liu and Hesterberg 2011, Cismasu et al., 2012, Cismasu et al., 2013, Manceau and Gates 2013, Hu et al., 2014, Massey et al., 2014, Johnston and Chrysochoou 2016, Namayandeh and Kabengi 2019). A previous study has shown that the incorporation of Al into lepidocrocite, another metastable iron oxyhydroxide mineral, distorts the local structure and morphologies, exposing faces with increased densities of active hydroxyls and consequently more adsorbed phosphate on the surface (Liao et al., 2020). Increasing Al content has also been shown to result in lower (more negative) $\Delta H_{ads,}$ and more sulfate adsorbed on Al-doped Fh (Namayandeh and Kabengi 2019).

The literature regarding the long-term transformation of Al-doped and Al–substituted Fhs is relatively sparse and remains variable in terms of experimental protocols. This gap has meant that AlFh aging pathways and their underlying mechanisms are much less understood than in their "pure" Fh counterparts. Schwertmann et al. (2000) conducted one of the few long-term (16 years) transformation studies on aging AlFh and found an incomplete transformation of Fh with only

peaks associated with Ht observed. The optimal pH value for the formation of Gt from pure Fh is 4; considering that the AlFh samples in this study were kept at a constant pH 4, one would expect Gt formation instead of Ht. This result underscores that not only does Al retards the overall transformation in Fh, but that it influences the underlying mechanisms involved. The authors posited that Al lowers the solubility of AlFh, which inhibits Gt formation since Fh dissolution is a necessary first step. The lack of other studies of the implications of Al incorporation on Fh's transformations upon aging highlights a need for a further systematic examination that encompasses a range of other conditions, particularly those that are environmentally relevant.

The purpose of this work is to investigate the role Al plays in influencing the transformation of aged Fh samples that vary in Al content and aging duration under aerobic conditions. We utilize a host of techniques, e.g. powder X-ray diffraction, flow microcalorimetry, drop solution microcalorimetry, X-ray adsorption spectroscopy, and X-ray magnetic circular dichroism spectroscopy, to determine the physical and chemical properties of these aged samples to assess differences in their aging. Most Fh found in environmental systems possess some degree of impurity, and the plethora of literature regarding the transformation and properties of Fh is derived from impurity-free Fh. Our results will be an important step toward a more realistic understanding of the multitude of ways Fh and AlFh affect our natural systems.

2.2 Materials and Methods

2.2.1 Sample Synthesis and Selection Criteria

Fh and AlFh samples were synthesized in the period spanning 2016-2018 for a previous study (Namayandeh and Kabengi 2019), according to a modified Schwertmann and Cornell's protocol (Cornell and Schwertmann 2003). In brief, 0.2 M $Fe(NO_3)_3$ and 0.2 M $Al(NO_3)_3$ solutions were proportionally mixed to obtain solutions at 0, 12, and 24 mol% Al. The mixed solutions were

titrated within 5 minutes to pH 7.50 ± 0.01 with a freshly prepared 1 M KOH solution, centrifuged and dialyzed against 18.2 MΩ water until the conductivity of the supernatant dropped below 20 uS.cm^{-1}. The resulting suspensions and samples, when dried, were denoted as 0AlFh (0 mol% Al), 12AlFh (12 mol% Al), and 24AlFh (24 mol% Al). Since their initial preparation, the suspensions have been stored aerobically in sealed containers. For this study, two sets of 0AlFh, 12AlFh, and 24AlFh samples were chosen to represent two aging durations. At the time of selection, one set has aged for 28 months and is denoted with an "_O" to designate an older age, e.g., 12AlFh_O for the 12AlFh sample in the set that aged longer for 28 months. The other set had aged for 16 months and is denoted by "_Y" to reference a younger age, e.g., 12AlFh_Y. This notation is maintained throughout the paper, even when the characterization experiment occurred at a later date. When required, unaged Fh and AlFh samples were synthesized following the same protocol as described above (Cornell and Schwertmann 2003). These samples are denoted by "_F" for fresh e.g., 12AlFh_F. As needed for the experiments, aliquots for all AlFh samples were dried under a fume hood for a minimum of 12 hours and ground into powders using a sterile agate mortar and pestle.

2.2.2 Physical Characterization

2.2.2.1 X-ray Diffraction

Bulk powder XRD was used to identify and quantify, as possible, all iron and aluminum phases present due to Fh phase transformation. All XRD patterns were acquired on a Panalytical XPert Pro (Malvern, United Kingdom) X-ray diffractometer using CuK-α radiation (45kV, 40mA radiation source, 5–70˚ 2-theta range, divergence slit size 1˚, step size 0.013˚) with a graphite monochromator to mitigate the effect of Fe fluorescence during analysis. Powdered samples were mounted on low-background sample holders with random-orientation. For semi-quantitative XRD

analysis (SQXRD), a Rietveld fitting was applied to the diffraction data collected for 0AlFh_O and 0AlFh_Y samples using the software, HighScore Plus (Panalytical, Malvern, United Kingdom) in order to generate phase proportions based on the phases identified during qualitative peak analysis. For parameterization of the Rietveld refinement, Gt (indexed PDF ICDD no. 98-007-1808) and Ht (indexed PDF ICDD no. 98-008-2136) were used as phases for the fitting. Background anchor points needed for the fitting were selected while allowing the software to automatically adjust the scale factor, zero shift, and lattice parameters to simulate the experimental diffraction data.

2.2.2.2 X-Ray Scattering and PDF analysis

Synchrotron-based X-ray total scattering data were collected on powdered dry 0AlFh samples at beamline 11-ID-B (58.7 keV, λ =0.2113 Å) at the Advanced Photon Source, Argonne National Laboratory. The integration of the raw scattering data into spectra was done using the xPDFsuite, the graphical interface for PDFgetX3 (Juhás et al., 2013). Background intensities were measured directly and subtracted from the sample data to generate I(Q) (i.e., intensity vs. Q-space, where $Q = 4\pi sine\theta/\lambda$). All data regardless of the extent of transformation were then normalized based on the chemical composition FeO(OH) to generate the total scattering structure function, S(Q). The S(Q) is then Fourier transformed, using Q_{max} = 25-26 A^{-1}, to generate the PDFs. A linear combination fitting (LCF) approach was used to quantify the proportions of Fh, Ht, Gt, and gibbsite (Gb) in each sample using the software WinXAS. Experimental PDFs for crystalline Gt, Ht, and/or Gb were used as LCF components. The PDFs for samples 0AlFh, 12AlFh, and 24AlFh were used as components for ferrihydrite in the pure, 12% Al, and 24% Al series, respectively.

2.2.2.3 Brunauer–Emmett–Teller (BET) Surface Area Analysis

Specific surface areas (SSA) of all samples were evaluated by conducting 7-point BET N_2 adsorption isotherms on a Quantachrome AS1Win, (Quantachrome Instruments, Boynton Beach, FL, USA). Before the measurements, the samples were degassed at 50 ºC for 15 hours. This low degassing temperature was necessary to prevent the removal of structural waters and hence, to mitigate the effects of any unintended transformation of the Fh samples into Ht with increasing temperatures (Cornell and Schwertmann 2003).

2.2.2.4 X-ray Adsorption Spectroscopy (XAS) and Magnetic Circular Dichroism (XMCD)

X-ray absorption near-edge spectroscopy data were collected at beamline BL6.3.1 at the Advanced Light Source Beamline in Berkeley, CA. Al and O K-edge spectra were collected at room temperature, and Fe L-edge spectra were collected at 20K. The X-ray absorption spectra were recorded in the total electron yield mode (TEY), and the XMCD spectra were determined by the difference in the incident beam intensity normalized x-ray absorption spectra between two oppositely polarized 0.9T magnetic fields.

2.2.2.5 Enthalpies of Formation and Water Content.

Four different 0AlFh samples, aged for 7, 13, 18, and 23 months were sent to the University of California, Davis, to acquire thermodynamic properties, namely enthalpies of drop solution and formation, from high-temperature oxide melt solution calorimetry measurement. Experiments were conducted using a fabricated Tian-Calvet twin calorimeter where the samples were hand-pressed loosely into pellets that were dropped from room temperature into molten $3Na_2O_4.MoO_3$ at 700ºC. Oxygen gas was flushed over the solvent at 51.6 mL/min and was bubbled through at 5.9 mL/min to hasten oxidation. Eight replicated measurements were performed for each sample.

The water content of each sample was obtained by thermogravimetric analyses Setaram Labsys Evo). Samples were heated from 25°C to 800°C at a rate of 10°K/min.

2.2.2.6 Surface Charge

Surface charge measurements were obtained via flow microcalorimetry. Custom-made flow microcalorimeters fabricated in the Kabengi laboratories at Georgia State University were used to measure the energies associated with chloride and nitrate exchange, i.e., Q_{exch}, on freshly synthesized and aged AlFh samples. The instrumentation and basic operational procedures have been detailed elsewhere and are summarized in Section S1 of the SI. The energies associated with reversible anionic exchange concur in reaction times and magnitudes (Kabengi et al., 2006) and can be used as an indirect proxy for the positive surface charge (Kabengi et al., 2017). Solutions of 0.05 M NaCl and $NaNO_3$ adjusted to a pH of 5.60 ± 0.01 were used. A known sample mass (~50 mg) was packed into the sample microholder and flushed with NaCl until a calorimetric baseline was established. Then, the input solution was changed to $NaNO_3$, and the calorimetric signal associated with chloride being replaced by nitrate [C/N] recorded. After the [C/N] exchange reaction has ended, as indicated by a return of the calorimetric signal to the original baseline, the solution was switched back to NaCl, and the calorimetric signal associated with nitrate being replaced by chloride [N/C] obtained. Multiple replicates of [C/N] and [N/C] exchanges were collected over several days until no detectable changes in the magnitude of the signal occurred.

Long-term pH measurements were taken for multiple sets of 0, 12, and 24%-AlFh samples that had been freshly synthesized and allowed to age in their mother liquor under aerobic conditions, in sealed benchtop storage. The measurement frequency varied from daily at the start of aging to weekly after the first 2 months, as changes in the pH were unfolding very slowly. The goal of these experiments is to assess the evolution of pH conditions over time, as this may provide information

regarding the mechanics underlying phase transformations. All samples were vigorously shaken, and pH meter calibration was performed prior to pH measurements (OrionStar A215 pH meter, Fisher Scientific).

2.3 Results

2.3.1 Characterization

2.3.1.1 Chemical composition and surface area

A summary of the chemical composition and BET-derived SSAs values of all the samples used in this study is shown in Table 2-1. Also included are representative values for 0AlFh, 12AlFh, and 24AlFh "parent" samples from the Namayandeh and Kabengi (2019) study. These samples were characterized when they were initially synthesized and, thus, are considered a benchmark for data from the aged samples used in this study. Upon aging, the SSA value of the 0AlFh_O sample decreased significantly by 78.4% from 368 ± 14 m^2/g to 79 m^2/g. The SSA value for the 0AlFh_Y sample also decreased by roughly 52.9% from 368 ± 14 m^2/g to 173 ± 16 m^2/g. Samples containing Al, i.e., 12AlFh_O, 12AlFh_Y, 24AlFh_O, and 24AlFh_Y, showed no significant changes in their measured surface areas. Given the expected inherent variation in synthesizing Fh and AlFh samples, and the lower degassing temperature used for the aged samples in this study, i.e., 50°C, as opposed to 150°C used on freshly synthesized samples in Namayandeh and Kabengi (2019), the observed fluctuations for only the aluminum-doped samples remain within experimental errors.

Table 2-1: The composition and specific surface areas (SSA) for aged 0, 12, and 24AlFh samples. The change in SSA was calculated by comparing values for aged (this study) and freshly synthesized AlFh samples (Namayandeh and Kabengi, 2019).

Sample Name	Target Al/Al+Fe (mol %)	Measured Al/Al+Fe (mol %)[1]	Surface area of aged samples (m^2/g) [a]	Surface area at time of synthesis[4] (m^2/g) [b]	Change in Specific Surface Area (%)[5]
0AlFh_O	0	0.02 (0.01)[2]	79[3]	368 (14)	-78.4
12AlFh_O	12	10.98 (0.09)	406 (40)	358 (20)	13.3
24AlFh_O	24	22.50 (0.40)	377 (308)	363 (24)	3.8
0AlFh_Y	0	0.02 (0.01)	173 (16)	368 (14)	-52.9
12AlFh_Y	12	10.98 (0.09)	384 (5)	358 (20)	7.2
24AlFh_Y	24	22.50 (0.40)	364 (20)	363 (24)	0.4

[1] Data in this column are averages of values for samples from Namayandeh and Kabengi (2019) and this study.
[2] Numbers in parentheses correspond to the standard error of the mean.
[3] One BET measurement was obtained for this sample
[4] Representative SSA values were taken from Namayandeh and Kabengi (2019) for freshly synthesized 0AlFh, 12AlFh, and 24AlFh samples.
[5] Data in this column are calculated as (Value in Column[b] – Value in Column[a])/(Value in Column[b]).

2.3.2 X-Ray Techniques

2.3.2.1 X-ray Diffraction

Bulk X-ray diffraction (XRD) patterns for the aged AlFh samples, i.e., 12AlFh_Y, 12AlFh_O, 24AlFh_Y, and 24AlFh_O were consistent with those of poorly crystalline 2-line Fh, with characteristic peaks occurring at 34 and 61 degrees 2-theta, albeit with slight peak broadening stemming from Al incorporation (Cornell and Schwertmann 2003, Jia et al., 2006) (Section 2.2 of SI). No other discernable Fe and Al phases were detected. Qualitative inspection of the diffraction patterns for both the 0AlFh_O and 0AlFh_Y samples showed evidence of transformation into Ht and Gt, based on reference sample peak positions and relative peak intensities. The samples became more crystalline with increased aging, as demonstrated by sharper and larger intensity diffraction peaks (Figure 2-1).

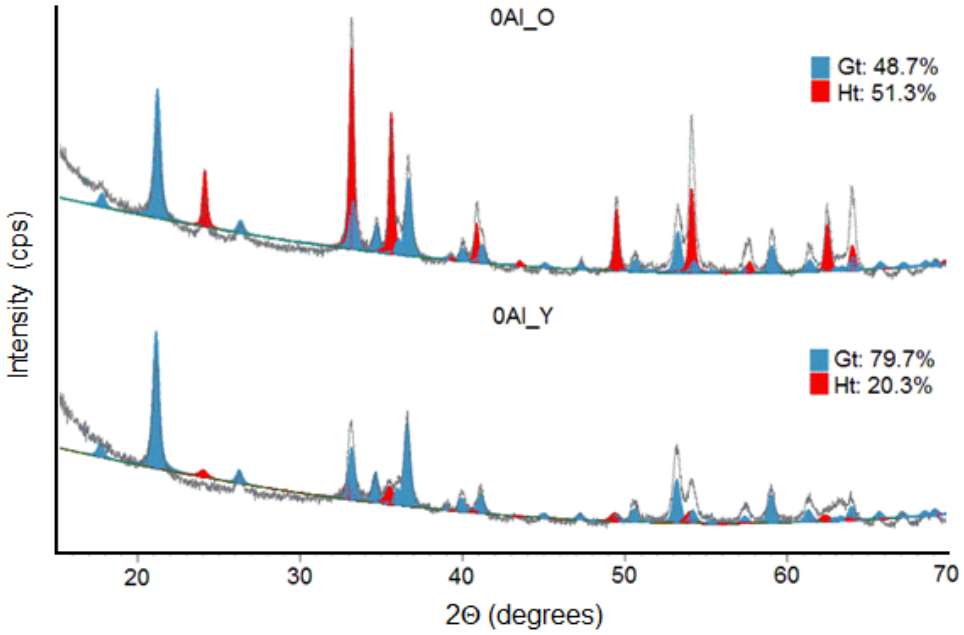

Figure 2-1: X-ray diffractograms for undoped Fh samples aged for 28 months (0AlFh_O) and 16 months (0AlFh_Y) overlaid with the Rietveld refinement fit showing the contribution of goethite (Gt: blue) and hematite (Ht: red).

To quantify the proportions of Ht and Gt in aged samples, we used Rietveld refinement to analyze the experimental XRD spectra of 0AlFh_O and 0AlFh_Y samples, as they were the only two samples with XRD detectable phase transformations (Figure 2-1). In the younger sample (~16 months), Gt is the dominant phase at 79.7%, while Ht accounted for 20.3% of all crystalline phases. With aging, more Ht forms. It accounts for 51.3% in the 0AlFh_O, while the Gt contribution drops to 48.7%. It was challenging to account for any remaining amorphous Fh due to the overlap of the characteristic peaks of Fh with Gt and Ht peaks, which were pronounced as 0AlFh had significant crystallization into these two phases. Therefore, a Fh phase was not used in the Rietveld refinements. Instead, we posited that fitting and subsequently removing the background signal during the refinement would suffice to account for the contribution of amorphous Fh. The difference between the calculated fit and experimental data can be seen in Section 2.2 of the SI.

2.3.2.2 X-ray Total Scattering

The structures of AlFh samples were probed further by conducting synchrotron-based X-ray total scattering. The background-subtracted total scattering, I(Q), obtained for both fresh and aged undoped samples, i.e., 0AlFh_F, 0AlFh_Y and 0AlFh_O, concurred with XRD data in that they revealed significant crystallization into Ht and Gt (Section 2.2 of the SI) upon aging. The contributions of each phase, along with that from the amorphous Fh phase, which is accessible from total scattering data, were obtained by performing a linear combination fitting (LCF) of phases present with the assumption that only Fh, Ht, and Gt are present (Figure 2-2). There are three key points to take away from these results. First, as Fh samples age and become more crystalline, the Gt proportion becomes less abundant. Gt accounts for 80% of all phases in the 0AlFh_Y but only 61% in the 0AlFh_O sample. Conversely, the proportion of Ht increases with aging time; its abundance increased by almost ten-folds from only 3% in the 0AlFh_Y to 33% in the 0AlFh_O sample. Second, Fh persists in the oldest sample and accounts for 6% despite more than 28 months of aging. This finding is consistent with results from another long-term aging study showing 2-19% residual amorphous Fh remaining after 970 days of aging at room temperature in pH conditions lower than pH 6 (Schwertmann and Murad 1983). The third point taken from the results in Figure 2-2 is that while bulk XRD and LCF-fitting of scattering data agreed on the decreasing Gt:Ht ratio trend with aging, the proportion of Gt and Ht in each sample differed significantly. We attribute the divergence of results to imperfect fitting of the background signal and Fh being excluded from the Rietveld refinement of the diffraction data.

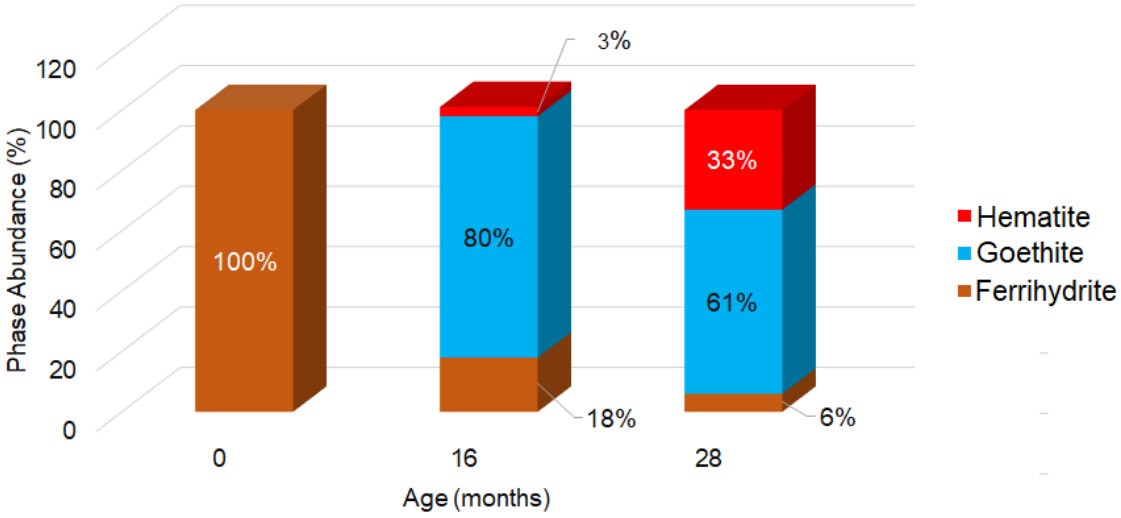

Figure 2-2: Abundance of hematite (red), goethite (blue), and ferrihydrite (brown) derived from a linear combination fitting of PDF data collected on freshly synthesized (0AlFh_F), and 16-months (0AlFh_Y) and 28-months (0AlFh_O) aged ferrihydrite samples.

While bulk-XRD data indicated that the presence of Al at both 12 and 24 mol% retards the aging-induced crystallization in Fh, an examination of the total scattering, I(Q), for Al-doped samples reveals additional nuances about the effect of Al in aged AlFh samples (Figure 2-3). We observe subtle, but clear, evidence for the beginning stages of crystalline product formation in both the 12AlFh_Y and 12AlFh_O samples, with the latter exhibiting enhanced peaks at ~2.9 Å and ~3.7 Å, positions correlated with Ht and Gt. These peaks, particularly the ~ 3.7 Å peak, are less pronounced in samples containing 24 mol% Al, although a slight showing of a peak at 2.9 Å is emerging in the 24AlFh_O. Furthermore, the dominant peak associated with gibbsite (Gb), ~1.25 $Å^{-1}$, can be seen in the 24AlFh samples with the feature becoming more pronounced with increasing sample age (Figure 2-3b). The upper limit of Al incorporation into Fh is understood to hover between 20 - 25 mol % Al (Schwertmann, 1978, Manceau et al., 2013) and hence the presence of Gb in samples containing 24 mol% is not surprising. Yet it is a welcome confirmation of the difference between 12 and 24 mol% Al impact of Fh's structure.

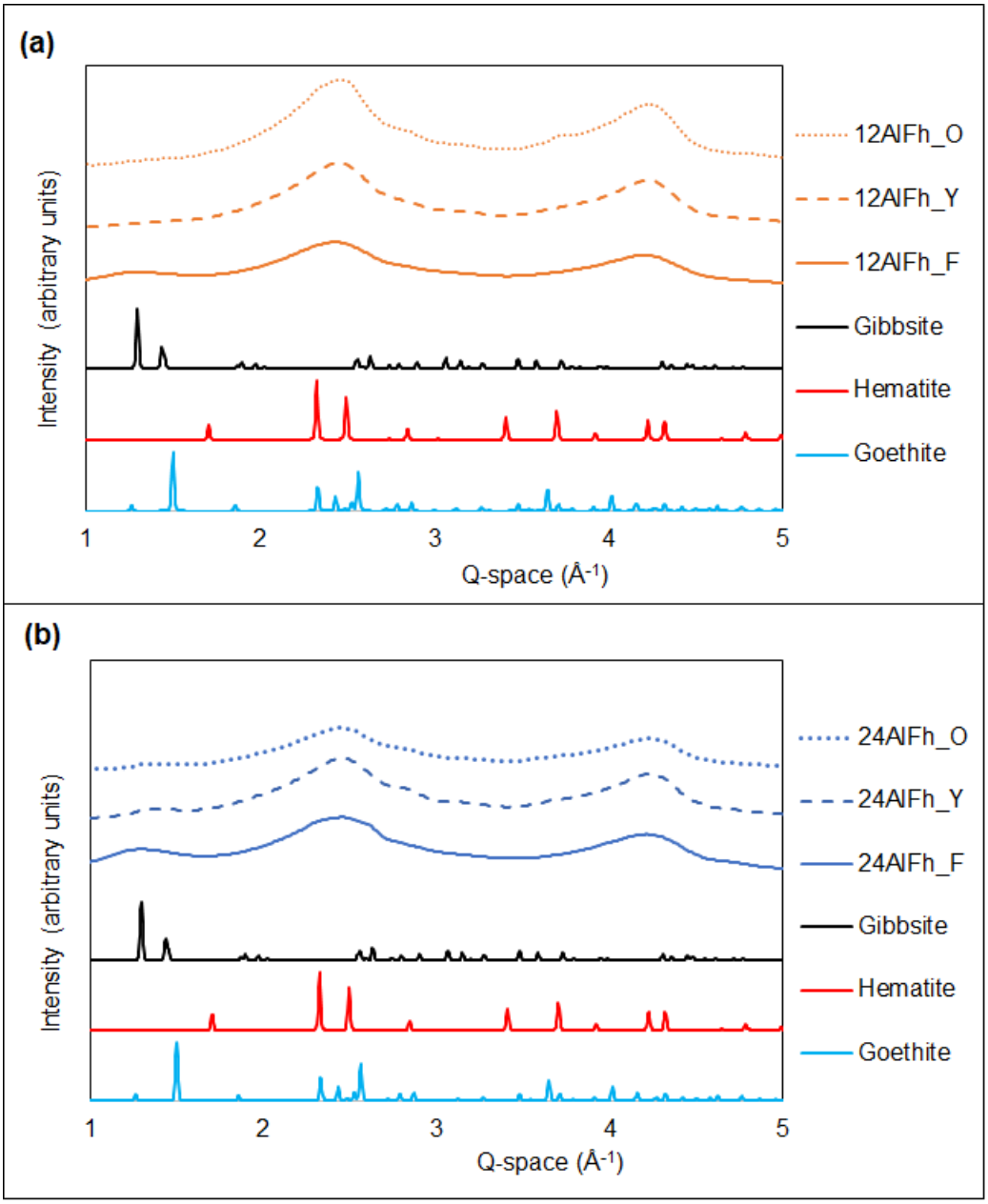

Figure 2-3: Background-subtracted total scattering, I(Q), for (a) 12AlFh samples; (b) 24AlFh samples with gibbsite, hematite, and goethite reference peaks are shown.

2.3.2.3 Long-term daily pH measurements

The transformation pathways of Fhs in unbuffered systems. into more crystalline phases are affected and accompanied by changes in pH stemming from the release of protons during transformation (Jambor and Dutrizac 1998, Cornell and Schwertmann 2003). To capture these

changes, and potentially correlate them to the other physical and structural properties being measured, we monitored the pH of the mother liquor in four sets of freshly synthesized 0AlFh, 12AlFh and 24 AlFh samples that had been aging for the last 8.5 months. These measurements showed a significant difference in the starting pH values (day 1) between undoped (0AlFh samples) and doped (12AlFh and 24AlFh) samples (Table 2-2). We measure an initial pH of 4.92 ± 0.16 for 0AlFh samples, 5.37 ± 0.10 for 12AlFh, and 5.43 ± 0.10 for 24ALFh samples. With time, pH values were slowly trending downwards with differences again between undoped and doped samples. The daily pH change value for 0AlFh samples was calculated to be -0.40 ± 0.012, while those for 12AlFh and 24AlFh were -0.026 ± 0.009 and -0.018 ± 0.006 respectively. The pH measurements go hand in hand with the observed transformation discussed above whereby undoped samples are witnessing the formation of Gt and, to a lesser extent Ht. It is important to note that the 0AlFh_Y and AlFh_O samples were aged for 16 and 28 months respectively, while the oldest set of samples for which pH measurements were obtained is 8.5 months old. We anticipate more dramatic changes in pH values as the transformation accelerates. Additional results presented in the section below place this breakthrough point between 13 and 15 months.

Table 2-2: The average initial pH post-synthesis and the pH change per day since synthesis for four replicate sets of 0, 12, and 24AlFh samples.

Sample Name	pH value at Day 1[1]	Daily pH Change[3]
0AlFh_F	4.92 (0.16)[2]	-0.40 (0.012)
12AlFh_F	5.37 (0.10)	-0.026 (0.009)
24AlFh_F	5.43 (0.10)	-0.018 (0.006)

[1] Average measurements of four sets of freshly synthesized 0, 12, and 24AlFh taken the first day after sample synthesis.
[2] Numbers in parentheses correspond to the standard error of the mean.
[3] Average slopes of the trendlines used to fit the pH values.

2.3.2.4 Enthalpies of Formation and Surface Energies

The tracking of the physical and structural transformations with aging was augmented by measurements of the enthalpies of formation (ΔH^o_f) and surface energies (ΔH_{DS}) by acid solution calorimetry. Before the collection of the thermodynamic data, thermogravimetric measurements ascertained the water content of each of the four aged 0AlFh samples (Table 2-3). The ΔH^o_f from binary oxides (α-Fe_2O_3; Ht) and H_2O ranged from 13.48 ± 1.14 kJ/mol to 29.32 ± 1.38 kJ/mol, highlighting the overall energetic metastability of these samples. Longer aging times, i.e., 18 and 23 months, corresponded to lower water content and less endothermic ΔH^o_f values, than shorter times, i.e., 13 and 7 months. A similar trend was observed when ΔH^o_f were calculated from elements, albeit with higher exothermic values ranging from -668.67 ± 1.92 kJ/mol to -784.49 ± 2.04 kJ/mol (Table 2-3).

Table 2-3: Enthalpies of drop solution and formation of undoped Fh aged for 7, 13, 18, and 23 months.

Sample Name	Formula n.H_2O[1]	ΔH_{DS}		ΔH^o_f	
		(kJ/mol)	(J/g)	$\Delta H^o_{f(elements)}$ (kJ/mol)	$\Delta H^o_{f(oxides)}$ (kJ/mol)
0Al_23mos	0.445	98.55 (1.32)[2]	1017.38 (13.61)	-668.67 (1.92)	14.46 (1.41)
0Al_18mos	0.456	100.28 (1.02)	1033.14 (10.55)	-672.73 (1.73)	13.48 (1.14)
0Al_13mos	0.799	108.13 (1.29)	1047.31 (12.46)	-755.07 (1.90)	29.32 (1.38)
0Al_7mos	0.891	117.69 (1.49)	1121.95 (14.23)	-784.49 (2.04)	26.09 (1.57)

[1] *Water content as samples are heated from 25°C to 800°C at a rate of 10K/min and is calculated based on $FeOOH{\cdot}nH_2O$ to match previously published thermodynamic data used in the calculation of ΔH^o_f.*
[2] *Numbers in parentheses correspond to the standard error of the mean.*

The nonlinear decrease in both $\Delta H^o f_{oxides}$ and $\Delta H^o f_{elements}$ presents the sharpest difference between 13 and 18 months of aging (Figure 2-4). This large difference within that time range points to a kinetically driven phase transformation that is accompanied by a loss of structural water consistent with the dehydration needed to facilitate Ht formation from Fh. Furthermore, the lower $\Delta H^o f$ and water content with increasing sample age indicate an increase in overall energetic stability, evidenced by the surface energy values that drop from 1121.95 ± 14.23 J/g for the shortest aging period to 1017.38 ± 13.61 for the longest (Table 2-3). These results concur with earlier evidence for a greater abundance of crystalline phases in aged Fh samples (Figure 2-1) and with surface area reductions, which is also observed in this study (Table 2-1). Previous studies on Ht and Gt also show a reduction in measured surface areas with decreasing water content (Mazeina et al., 2005, Mazeina and Navrotsky 2007).

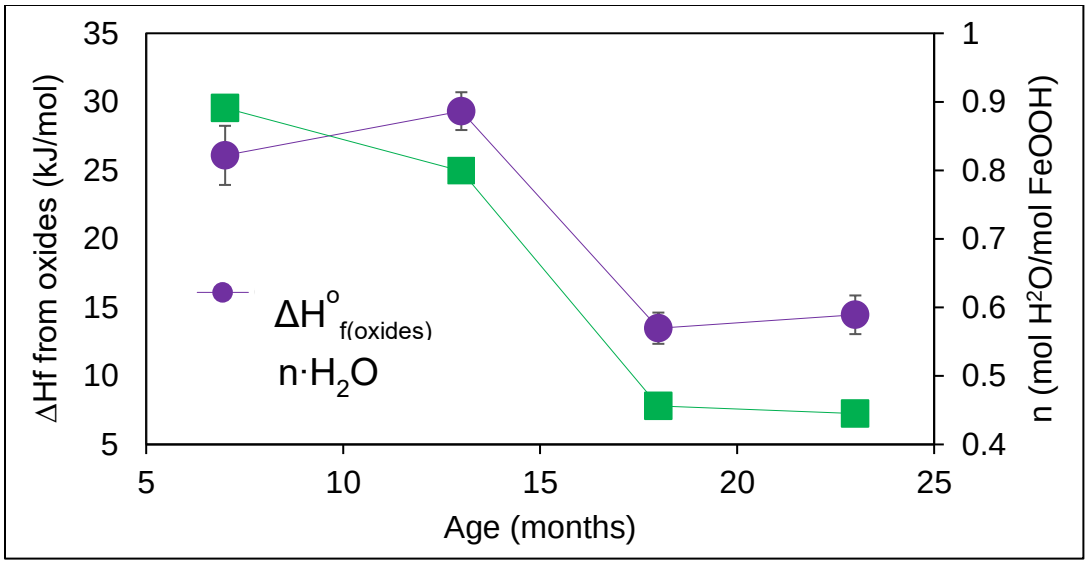

Figure 2-4: Plot of the enthalpies of formation from α-Fe_2O_3 (primary y-axis) and water content (secondary y-axis) as a function of sample age for undoped ferrihydrites samples.

2.3.2.5 Anion Exchange Energies as a Probe of Surface Charge

Figure 2-5 shows representative raw data (calorimetric signals versus time) for [C/N] and [N/C] exchanges that were obtained on the 0AlFh, 12AlFh, and 24AlFh samples aged for 16 and 28 months. For all samples, [C/N] was exothermic and [N/C] endothermic. The measured enthalpic signs were consistent with previous studies on ferrihydrites (Kabengi et al., 2017, Namayandeh and Kabengi 2019) and other metal oxides (Kabengi et al., 2006, Situm et al., 2017). A visual inspection reveals that the incorporation of Al results in larger calorimetric peaks while aging in the absence of Al results in significantly smaller peaks.

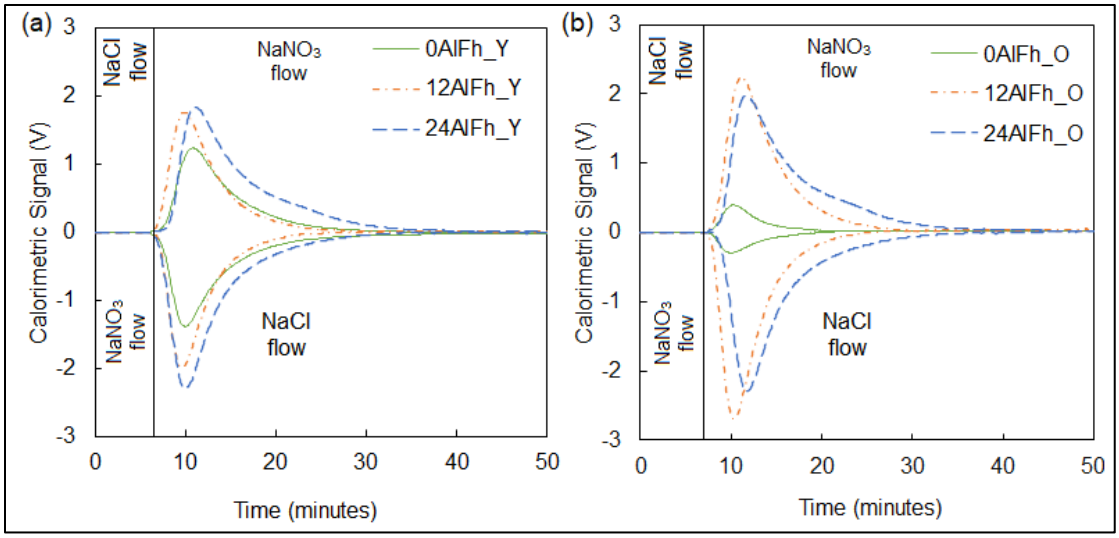

Figure 2-5: Representative calorimetric signals for Cl^- and NO^{3-} exchanges for 0AlFh, 12AlFh, and 24AlFh samples aged for (a) 16 months and (b) 28 months. A positive peak corresponds to an exothermic reaction and a negative peak, an endothermic reaction.

The normalized Q_{exch} values (mJ/mg) obtained from integrating the calorimetric signals presented in Figure 2-5 are presented in Table 2-4. Consistent with previous work (Kabengi et al., 2006, Namayandeh et al., 2019), the magnitude of Q_{exch} for [C/N] and [N/C] was the same highlighting the reproducibility and reversibility of [N/C] and [C/N] exchange reactions that can thus, be used as a proxy for the positive charge of the samples.

Table 2-4: The heat of exchange values for nitrate replacing chloride [C/N] and chloride replacing nitrate [N/C] reactions for 16 months (_Y) and 28 months (_O) old ferrihydrites samples with 0, 12, and 24 mol % aluminum doping.

Sample Name	Q_{exch} (mJ/mg)		Q_{exch} (mJ/m^2)	
	[N/C]	[C/N]	[N/C]	[C/N]
0AlFh_Y	2.23 (0.09)[1]	-2.30 (0.11)	11.19 (0.45)	-11.50 (0.55)
12AlFh_Y	3.28(0.09)	-3.49 (0.07)	8.53 (0.74)	-9.10 (0.18)
24AlFh_Y	2.92 (0.04)	-2.96 (0.02)	8.00 (0.10)	-8.08 (0.05)
0AlFh_O	0.46 (0.02)	-0.53 (0.01)	5.71 (0.23)	-6.66 (0.13)
12AlFh_O	4.00 (0.05)	-4.12 (0.05)	9.20 (0.11)	-9.48 (0.12)
24AlFh_O	3.35 (0.03)	-3.44 (0.06)	8.90 (0.07)	-9.14 (0.16)

[1] *Numbers in parentheses correspond to the standard error of the mean.*

Undoped 0AlFh samples had lower Q_{exch} values compared to both 12AlFh and 24AlFh samples reflecting the greater abundance of crystalline phases that have lower SSA in the absence of Al. Furthermore, the mass-normalized Q_{exch} for both [C/N] and [N/C] on 0AlFh_O was 79% smaller than the values obtained for 0AlFh_Y. In the presence of Al and in both old and young sets, the highest value of Q_{exch} was observed for the 12AlFh samples. This trend is inconsistent with that observed in a similar study that reported an increase in the energetics of exchange reactions with increasing Al concentration in freshly synthesized ferrihydrites samples (Namayandeh and Kabengi 2019). This divergence in mass-normalized Q_{exch} from the previously characterized trend may be attributed to the lowering of the overall SSA present in 24AlFh samples, most likely due to the lower SSA of gibbsite relative to Fh (Van Emmerik et al., 2007).

2.3.2.6 X-ray Absorption Spectroscopy and X-ray Magnetic Circular Dichroism

A hallmark of the Michel model of ferrihydrite (Michel et al., 2007) is the presence of tetrahedral Fe(III) that imparts a unique XMCD spectral signature to Fh samples. Previous spectroscopic work on iron oxides (Guyodo et al., 2012) has shown the dominant spectral signatures for octahedral Fe(II), tetrahedral Fe(III), and octahedral Fe(III) appearing at

approximately 707 eV, 708 eV, and 710 eV respectively (Figure 2-6). Furthermore, Cismasu et al. (2012) observed substituted Al in octahedral coordination, and therefore an analysis of the tetrahedral to the octahedral spectral signatures can prove valuable in deciphering the effect of Al and aging on the Fh structure.

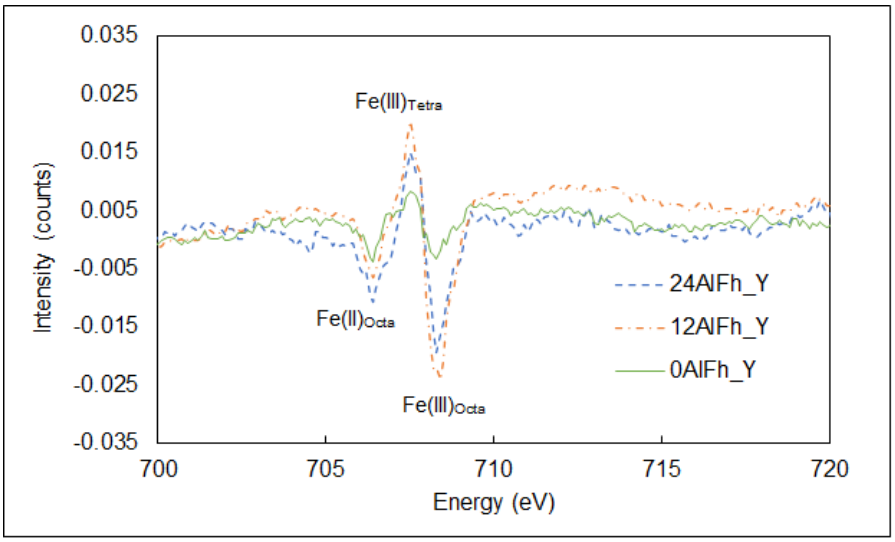

Figure 2-6: Fe L-edge XMCD spectra of 16-month-old 0AlFh_Y, 12AlFh_Y, and 24AlFh_Y samples. The spectral contributions of octahedral Fe(II), tetrahedral Fe(III), and octahedral Fe(III) are indicated.

Increasing Al content resulted in an increase in the magnetic moment of Fe present, evidenced by the overall larger magnitude of intensity from the XMCD spectra. Furthermore, there was an increase in the tetrahedral Fe(III):octahedral Fe(III) fraction with the incorporation of Al. There is an increase in the magnitude of the peak observed at approximately 707 eV, which is associated with tetrahedral Fe(III) in the Fe L-edge spectra, with increasing Al content. This may point to a depletion in octahedrally coordinated Fe(III), and will increase the tetrahedral Fe(III) to octahedral Fe(III) ratio. It is important to note that the intensity in the Fe(II) octahedral region is due to contributions from the Fe(III) octahedral and tetrahedral components, rather than the presence of Fe(II) (Pattrick et al., 2002).

The magnetic intensity of 0AlFh was seen to decrease with increasing sample age, whereas Al-doped samples did not show such a trend; both the 16-month-old AlFh samples showed similar spectra compared to their corresponding older counterparts (Section 2.3 of the SI). We interpret these as indicative that Al is "freezing" the magnetic structure of AlFh compared to pure Fh. Perhaps in the aged 0AlFh samples, over time there is a net reduction in magnetism due to preferential ordering of magnetic dipoles within the structure to cancel out the overall net dipole moment.

2.4 Discussion

2.4.1 Aging

Taken all together, the results from the physical, structural, and chemical characterization offer a comprehensive picture of the effect of aging and Al doping on the transformation of ferrihydrites. Consistent with previous studies (Schwertmann and Murad 1983, Jambor and Dutrizac 1998, Majzlan et al., 2004, Hansel et al., 2005, Zhang et al., 2018) and as expected, upon aging, undoped ferrihydrites underwent significant crystallization to form Gt and Ht phases. Both bulk XRD and synchrotron-based X-ray scattering data reveal a greater abundance of Gt in the 16-months aged sample (0AlFh_Y) than in the older 28-months aged sample (0AlFh_O). Conversely, Ht abundance increased with aging. The absolute magnitude of each phase differed depending on whether we accounted for the ~ 6-18% remaining amorphous Fh phase, which persisted despite 28 months of aging.

The limited studies on the transformation mechanisms and rates of ferrihydrites (Schwertmann et al., 2004, Das et al., 2011) have been conducted predominantly at a constant pH, i.e., as the suspensions were left to age they were periodically adjusted to maintain the chosen pH value. This difference in protocol constitutes a major obstacle to contrasting our results with those

previously reported. Nevertheless, looking at the study closest to our work in that it encompassed experiments conducted at 25°C and pH 7 (Das et al., 2011), another major point of divergence emerges in our results. Das et al. (2011) characterized Fh transformation as a two-stage process where Gt serves as an early intermediate phase for the transformation to Ht. With extended aging, their study saw the Gt peaks decrease while those for Ht increase. Even at pH and temperature conditions for which both phases occurred simultaneously, only a maximum of 10% Gt forms. Our results offer a different perspective. An examination of the XRD patterns and phase abundances presented in Figure 2-1 reveals that Gt forms before Ht. With increasing age, the Ht peaks increase in intensity, yet no apparent reduction in Gt peaks can be observed. We interpret these results to suggest that the dissolution-reprecipitation of Gt from Fh may be occurring at a similar rate to the solid-state transformation of Gt to Ht. This would result in the absolute amount of Gt in the system remaining similar however the proportion of Ht would increase and that of Ft decrease. The linear combination fitting of PDF data showed that almost 18% of amorphous Fh remained in the samples aged for 16 months. At some point prior to 16 months of aging, the conditions necessary for Ht formation became more favorable. The thermodynamic and thermogravimetric data further refine this suggested timeline and suggest an inflection point when Ht formation could potentially take precedence over Gt formation at around the 13-month mark. The synthesis protocol followed in this study resulted in an average initial pH value of 4.92 ± 0.16, and hence the acidic conditions could have favored Gt formation. Albeit for only 8.5 months, the long-term pH measurements are trending downward, and as the pH values become more acidic, Gt formation will more likely be enhanced (Schwertmann and Murad 1983). Kukkadapu et al. (2003) report a similar trend whereby, after 41 months of aging under aerobic conditions, the pH value of their unbuffered undoped Fh suspension dropped from 7.2 to 2.9. The authors also report a lower pH decrease over

time (from pH 7.2 to 5.0) in Ni-doped Fh suspensions that aged for 35 months, consistent with findings in this study for Al-doped samples (Kukkadapu et al., 2003). Results from X-ray magnetic circular dichroism (Figure 2-6, Section S2.3 of the SI) showed that with increased aging, the magnetic intensity of 0AlFh samples drastically decreased. This could be the result of unpaired magnetic moments stemming from tetrahedral and octahedral Fe, over time being magnetically ordered as this would reduce net magnetic dipole moment. In contrast, the magnetic intensities of Al-doped Fhs barely changed with increasing age. Al seems to be magnetically stabilizing or "freezing" the Fe atoms within Fh and preventing a gradual dipole orientation. Additionally, for Al-doped samples, the relative XMCD spectral contributions of octahedral Fe(II), tetrahedral Fe(III), and octahedral Fe(III) components did appear to vary over time. As we discuss below, quantification of each of these components via a linear combination fitting of the XMCD data provides insight into which Fe site is being potentially replaced by Al.

2.4.2 Aluminum doping

The presence of Al unequivocally retards the transformation of Fh into other crystalline phases. This result was evident from measurements of surface areas that remained unchanged for samples containing 12 and 24 mol% Al even after 28 months of aging. It was also clear from XRD patterns that did not differ much from that of 2-line Fh, with the exception of peak broadening that is typical for AlFh samples (Schwertmann et al., 2000, Cornell and Schwertmann 2003, Jentzsch and Penn 2006, Hansel et al., 2011). Evidence for gibbsite formation appeared in the X-ray total scattering spectra of aged samples as the Al increases from 12 to 24 mol% and provide yet another confirmation for the 24 mol% upper limit of Al structural incorporation into Fh (Schwertmann et al., 1979, Masue et al., 2007, Cismasu et al., 2012). With increased incorporation of Al, the XMCD data registered an increase in the ratio of tetrahedral Fe(III) to octahedral Fe(III) spectral

signatures. This decrease is namely due to a reduction in the signal of octahedral Fe(III), which seems to be the location of the Al substitution. We posit that as Al is incorporated into the surface, it prevents the dissolution of Fe(III) and inhibits Gt formation. This effect had been reported earlier whereby the rate of goethite dissolution was lower in the presence of Al (Schwertmann 1984).

2.4.3 Surface Charge

The lower mass-normalized Q_{exch} in 0AlFh_O versus 0AlFh_Y reflects the surface area reduction that results from the Fh transformation into less reactive Gt and Ht phases. In the presence of Al, and in both 12AlFh and 24AlFh samples, Q_{exch} was greater for older samples. Upon aging, a gibbsite phase starts to appear, as observed for the 24AlFh_O, and with a potentially higher pH ZPC, the new phase may result in a more positive surface charge. The same explanation can be at play for the 12AlFh. Even though no gibbsite phase was detected by either bulk XRD or total X-ray scattering, it is not impossible for the surface to have "gibbsite-like" islands that may result in a more positively charged surface relative to pure Fh. Namayandeh and Kabengi (2019) showed an increase in Q_{exch} with increasing Al content (Q_{exch}: 0AlFh < 12AlFh < 24AlFh) whereas the trend observed in this study was Q_{exch}: 0AlFh < 24AlFh < 12AlFh. The magnitude of Q_{exch} for the aged 12AlFh samples was consistently higher than the corresponding aged 24AlFh samples. This discrepant result necessitates further experiments to confirm this trend.

2.5 Significance and Conclusion

In this work, we explore the effect of aging duration and Al-doping on the transformations of AlFh. Total X-ray scattering and powder X-ray diffraction showed evidence of significant phase transformation occurring in undoped or pure 0AlFh samples, with crystallinity increasing over time. Gt and Ht were the two transformation products evident in both 0AlFh, with an increase in the proportion of Ht to Gt with increasing sample age. Based on the decrease of the periodic pH

measurements taken over the course of 8.5 months of aging suspensions, one would expect the secondary transformation of Fh into Gt. The appearance of Ht is thus favored by other factors, such as the observed decrease in water content with increasing sample age. The calorimetric results from [C/N] and [N/C] cycles on the 0AlFh samples reflected this phase transformation as the Q_{exch} values were lower with increased aging. At any given age, both 12AlFh and 24AlFh showed significantly larger Q_{exch} compared to pure 0AlFh. However, the Q_{exch} and specific surface area of 12AlFh and 24AlFh did increase with increasing sample age. Very few studies have attempted to look at the long-term implications of Al substitution into ferrihydrites. This work highlighted significant differences in the aging of undoped and doped AlFh. Considering that environmental conditions impose long-term variability in factors such as sample exposure duration, pH, etc. it is imperative to incorporate complexity into the way we think about Fh and AlFh behavior in natural systems. The prevalence of Al in environmental systems, and ultimately its affinity for substitution into Fh underscores how these results are needed for better modeling and predictions of Fh behavior under a broader range of complex and more realistic environmental conditions.

2.6 Acknowledgments

I would like to acknowledge Dr. Marc Michel for helping obtain and interpret X-ray total scattering data; Dr. Kevin Rosso and Dr. Carolyn Pearce for helping to obtain and interpret the XAS and XMCD data; and Dr. Alexandra Navrotsky and Andy Lam for helping generate and interpret results from acid solution calorimetry. I would like to acknowledge Dr. Daniel Gebregiorgis for his help with the collection of powder XRD data. I would also like to acknowledge Brianne Martin and Gabrial Goldner for their work on the microcalorimetric data collection.

REFERENCES

Bazilevskaya, E., D. D. Archibald, M. Aryanpour, J. D. Kubicki and C. E. Martínez (2011). "Aluminum coprecipitates with Fe (hydr)oxides: Does isomorphous substitution of Al3+ for Fe3+ in goethite occur?" Geochimica et Cosmochimica Acta **75**(16): 4667-4683.

Burleson, D. J. and R. L. Penn (2006). "Two-step growth of goethite from ferrihydrite." Langmuir **22**(1): 402-409.

Cismasu, A. C., C. Levard, F. M. Michel and G. E. Brown (2013). "Properties of impurity-bearing ferrihydrite II: Insights into the surface structure and composition of pure, Al- and Si-bearing ferrihydrite from Zn(II) sorption experiments and Zn K-edge X-ray absorption spectroscopy." Geochimica et Cosmochimica Acta **119**: 46-60.

Cismasu, A. C., F. M. Michel, J. F. Stebbins, C. Levard and G. E. Brown (2012). "Properties of impurity-bearing ferrihydrite I. Effects of Al content and precipitation rate on the structure of 2-line ferrihydrite." Geochimica et Cosmochimica Acta **92**: 275-291.

Cornell, R. M. and U. Schwertmann (2003). The iron oxides: structure, properties, reactions, occurrences and uses, John Wiley & Sons.

Cudennec, Y. and A. Lecerf (2006). "The transformation of ferrihydrite into goethite or hematite, revisited." Journal of Solid State Chemistry **179**(3): 716-722.

Das, S., M. J. Hendry and J. Essilfie-Dughan (2011). "Transformation of Two-Line Ferrihydrite to Goethite and Hematite as a Function of pH and Temperature." Environmental Science & Technology **45**(1): 268-275.

Ekstrom, E. B., D. R. Learman, A. S. Madden and C. M. Hansel (2010). "Contrasting effects of Al substitution on microbial reduction of Fe(III) (hydr)oxides." Geochimica et Cosmochimica Acta **74**(24): 7086-7099.

Guyodo, Y., P. Sainctavit, M. A. Arrio, C. Carvallo, R. L. Penn, J. J. Erbs, B. S. Forsberg, G. Morin, F. Maillot and F. J. G. Lagroix, Geophysics, Geosystems (2012). "X-ray magnetic circular dichroïsm provides strong evidence for tetrahedral iron in ferrihydrite." **13**(6).

Hansel, C. M., S. G. Benner and S. Fendorf (2005). "Competing Fe (II)-induced mineralization pathways of ferrihydrite." Environmental Science & Technology **39**(18): 7147-7153.

Hansel, C. M., D. R. Learman, C. J. Lentini and E. B. Ekstrom (2011). "Effect of adsorbed and substituted Al on Fe(II)-induced mineralization pathways of ferrihydrite." Geochimica et Cosmochimica Acta **75**(16): 4653-4666.

Hu, Y., Q. Li, B. Lee and Y. S. Jun (2014). "Aluminum affects heterogeneous Fe(III) (Hydr)oxide nucleation, growth, and ostwald ripening." Environ Sci Technol **48**(1): 299-306.

Jambor, J. L. and J. E. Dutrizac (1998). "Occurrence and Constitution of Natural and Synthetic Ferrihydrite, a Widespread Iron Oxyhydroxide." Chemical Reviews **98**(7): 2549-2586.

Jentzsch, T. L. and R. L. Penn (2006). "Influence of Aluminum Doping on Ferrihydrite Nanoparticle Reactivity." The Journal of Physical Chemistry B **110**(24): 11746-11750.

Jia, Y., L. Xu, Z. Fang, G. P. J. E. s. Demopoulos and technology (2006). "Observation of surface precipitation of arsenate on ferrihydrite." **40**(10): 3248-3253.

Johnston, C. P. and M. Chrysochoou (2016). "Mechanisms of Chromate, Selenate, and Sulfate Adsorption on Al-Substituted Ferrihydrite: Implications for Ferrihydrite Surface Structure and Reactivity." Environ Sci Technol **50**(7): 3589-3596.

Juhás, P., T. Davis, C. L. Farrow and S. J. J. J. o. A. C. Billinge (2013). "PDFgetX3: a rapid and highly automatable program for processing powder diffraction data into total scattering pair distribution functions." **46**(2): 560-566.

Kabengi, N. J., M. Chrysochoou, N. Bompoti and J. D. Kubicki (2017). "An integrated flow microcalorimetry, infrared spectroscopy and density functional theory approach to the study of chromate complexation on hematite and ferrihdyrite." Chemical Geology **464**: 23-33.

Kabengi, N. J., R. D. Rhue and S. H. J. S. s. Daroub (2006). "Using flow calorimetry to determine the molar heats of cation and anion exchange and the point of zero net charge on amorphous aluminum hydroxides." **171**(1): 13-20.

Kukkadapu, R. K., J. M. Zachara, J. K. Fredrickson, S. C. Smith, A. C. Dohnalkova and C. K. Russell (2003). "Transformation of 2-line ferrihydrite to 6-line ferrihydrite under oxic and anoxic conditions." American Mineralogist **88**(11-12): 1903-1914.

Liao, S., X. Wang, H. Yin, J. E. Post, Y. Yan, W. Tan, Q. Huang, F. Liu and X. Feng (2020). "Effects of Al substitution on local structure and morphology of lepidocrocite and its phosphate adsorption kinetics." Geochimica et Cosmochimica Acta.

Liu, Y. T. and D. Hesterberg (2011). "Phosphate bonding on noncrystalline Al/Fe-hydroxide coprecipitates." Environ Sci Technol **45**(15): 6283-6289.

Majzlan, J., A. Navrotsky and U. Schwertmann (2004). "Thermodynamics of iron oxides: Part III. Enthalpies of formation and stability of ferrihydrite (∼Fe(OH)3), schwertmannite (∼FeO(OH)3/4(SO4)1/8), and ε-Fe2O3 1 1Associate editor: D. Wesolowski." Geochimica et Cosmochimica Acta **68**(5): 1049-1059.

Manceau, A. and W. P. Gates (2013). "Incorporation of Al in iron oxyhydroxides: implications for the structure of ferrihydrite." Clay Minerals **48**(3): 481-489.

Massey, M. S., J. S. Lezama-Pacheco, F. M. Michel and S. Fendorf (2014). "Uranium incorporation into aluminum-substituted ferrihydrite during iron(ii)-induced transformation." Environ Sci Process Impacts **16**(9): 2137-2144.

Masue, Y., R. H. Loeppert and T. A. Kramer (2007). "Arsenate and Arsenite Adsorption and Desorption Behavior on Coprecipitated Aluminum:Iron Hydroxides." Environmental Science & Technology **41**(3): 837-842.

Mazeina, L., A. J. C. Navrotsky and C. Minerals (2005). "Surface enthalpy of goethite." **53**(2): 113-122.

Mazeina, L. and A. J. C. o. M. Navrotsky (2007). "Enthalpy of water adsorption and surface enthalpy of goethite (α-FeOOH) and hematite (α-Fe2O3)." **19**(4): 825-833.

Michel, F. M., L. Ehm, S. M. Antao, P. L. Lee, P. J. Chupas, G. Liu, D. R. Strongin, M. A. A. Schoonen, B. L. Phillips and J. B. Parise (2007). "The Structure of Ferrihydrite, a Nanocrystalline Material." Science **316**(5832): 1726-1729.

Namayandeh, A. and N. Kabengi (2019). "Calorimetric study of the influence of aluminum substitution in ferrihydrite on sulfate adsorption and reversibility." J Colloid Interface Sci **540**: 20-29.

Namayandeh, A., N. J. J. o. c. Kabengi and i. science (2019). "Calorimetric study of the influence of aluminum substitution in ferrihydrite on sulfate adsorption and reversibility." **540**: 20-29.

Pattrick, R. A., G. Van Der Laan, C. M. B. Henderson, P. Kuiper, E. Dudzik and D. J. J. E. J. o. M. Vaughan (2002). "Cation site occupancy in spinel ferrites studied by X-ray magnetic circular dichroism: developing a method for mineralogists." **14**(6): 1095-1102.

Schwertmann, U. (1984). "The influence of aluminium on iron oxides: IX. Dissolution of Al-goethites in 6 M HCl." Clay Minerals **19**(1): 9-19.

Schwertmann, U., R. Fitzpatrick, R. Taylor and D. Lewis (1979). "The influence of aluminum on iron oxides. Part II. Preparation and properties of Al-substituted hematites." Clays and Clay Minerals **27**(2): 105-112.

Schwertmann, U., J. Friedl, H. Stanjek and D. G. Schulze (2000). "The effect of Al on Fe oxides. XIX. Formation of Al-substituted hematite from ferrihydrite at 25 C and pH 4 to 7." Clays and Clay Minerals **48**(2): 159-172.

Schwertmann, U. and E. Murad (1983). "Effect of pH on the formation of goethite and hematite from ferrihydrite." Clays and Clay Minerals **31**(4): 277-284.

Schwertmann, U., H. Stanjek and H.-H. J. C. M. Becher (2004). "Long-term in vitro transformation of 2-line ferrihydrite to goethite/hematite at 4, 10, 15 and 25 C." **39**(4): 433-438.

Situm, A., M. A. Rahman, N. Allen, N. Kabengi and H. A. J. T. J. o. P. C. A. Al-Abadleh (2017). "ATR-FTIR and Flow Microcalorimetry Studies on the Initial Binding Kinetics of Arsenicals at the Organic–Hematite Interface." **121**(30): 5569-5579.

Van Emmerik, T. J., D. E. Sandström, O. N. Antzutkin, M. J. Angove and B. B. J. L. Johnson (2007). "31P solid-state nuclear magnetic resonance study of the sorption of phosphate onto gibbsite and kaolinite." **23**(6): 3205-3213.

Zhang, D., S. Wang, Y. Wang, M. A. Gomez, Y. Duan and Y. Jia (2018). "The Transformation of Two-Line Ferrihydrite into Crystalline Products: Effect of pH and Media (Sulfate versus Nitrate)." ACS Earth and Space Chemistry **2**(6): 577-587.

SUPPLEMENTARY INFORMATION FOR CHAPTER 2

Section S2.1: Instrumentation and basic operational procedure for the flow microcalorimeter

The flow microcalorimeter consists of a glass microcolumn apparatus with a sample holder into which a known mass of the sample is packed. A solution containing the chemical species of interest is flushed through the packed microcolumn at a controlled flow rate, which is continuously monitored and adjusted as needed to remain constant between 0.30 to 0.330 ml min^{-1}), until the thermal equilibrium is obtained as evidenced by a steady calorimetric baseline. The input solution is switched to another solution of a different composition e.g., pH, ionic strength, or concentration, and the change in the solution temperature resulting from either heat produced or consumed as the solute interacts with the solid is monitored. A pair of thermistors one upstream and one downstream from the sample holder, form one half of an electronic bridge that senses the temperature of the solution and generates an electrical signal. This calorimetric signal is displayed graphically and recorded as a function of time. The end of the reactions is observed when the calorimetric signal return to the initial thermal baseline. The peak areas are obtained by integrating the calorimetric peak relative to flow rate. The heats of reactions (Q in mJ/mg of packed solid) are calculated by converting the peak areas to energy units (J) using peaks of known energy input generated from a calibrating resistor located in the flow stream near the microsample holder. Figure S2.1.1 shows a series of heat pulses and the associated calibration curve.

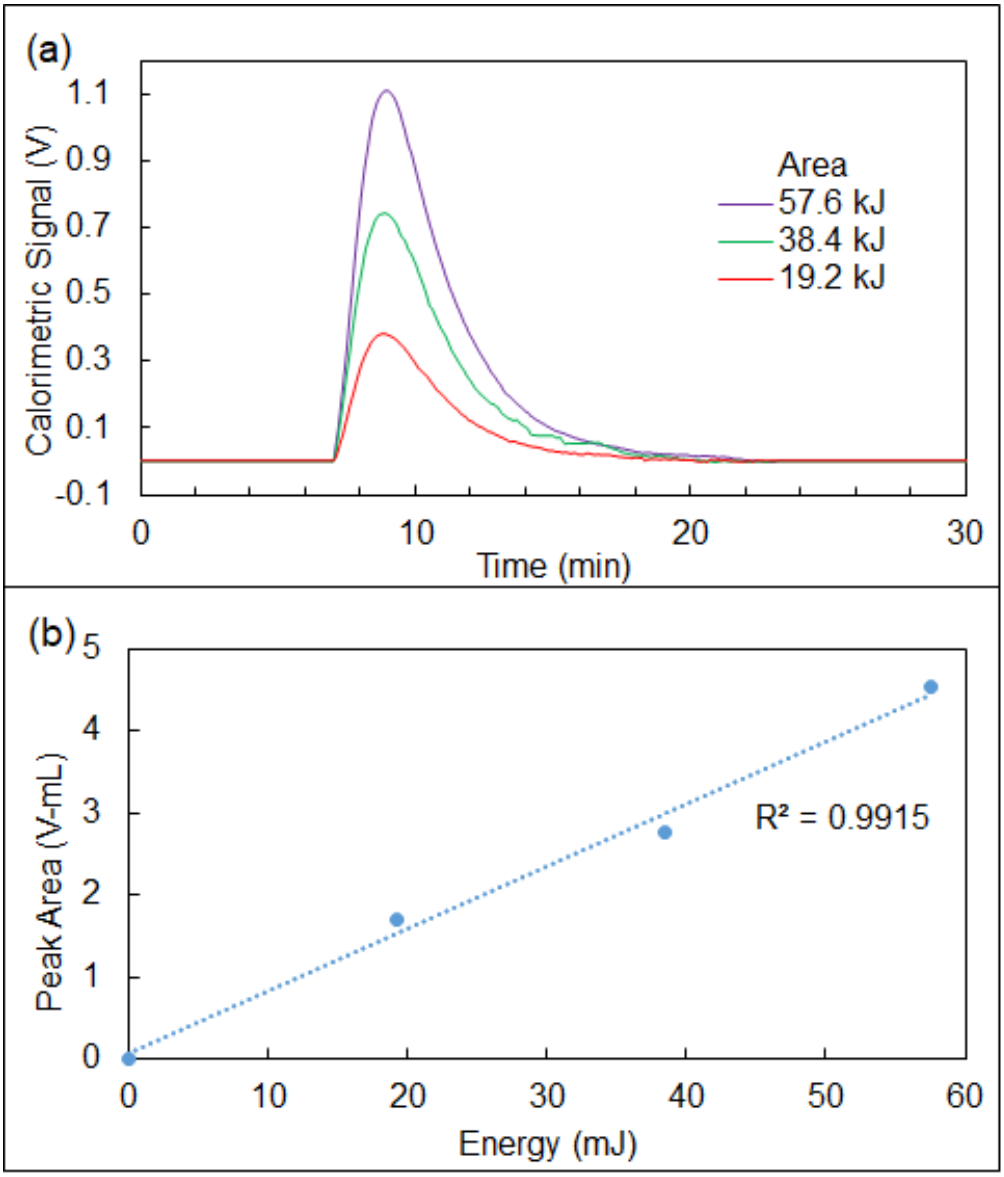

Figure S2.1.1: *Peaks obtained from a series of times heat pulses (top) and the corresponding calibration curves (bottom).*

Section S2.2: Bulk X-ray diffraction patterns, Rietveld refinement fitting, and Total X-ray Scattering

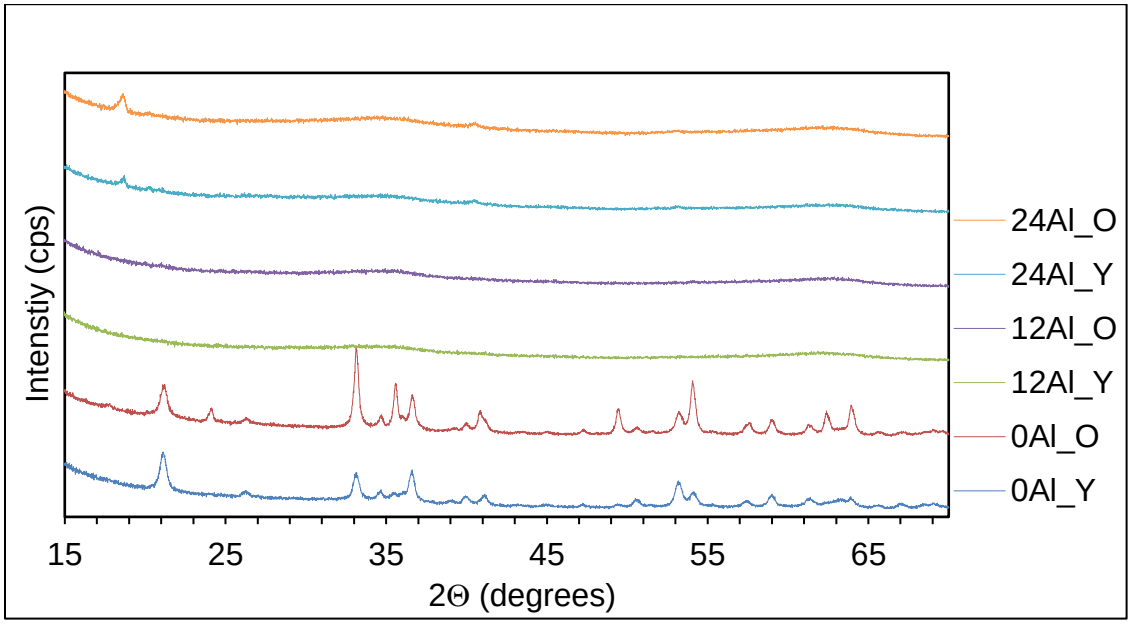

Figure S2.2.2: *X-ray diffractograms of aged (roughly 16 months and 28 months) ferrihydrites with 0, 12, and 24 mol % Al.*

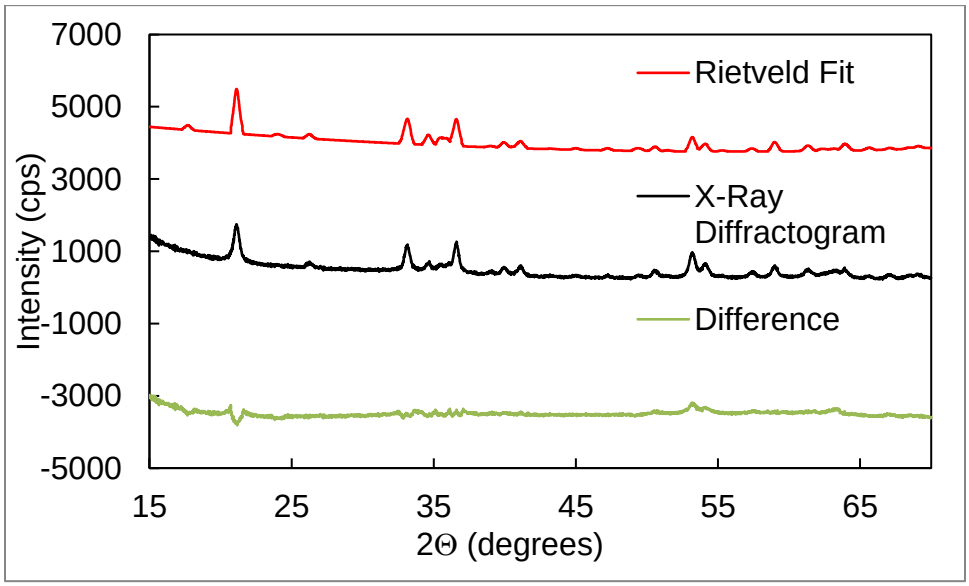

Figure S2.2.3: *Experimental X-ray diffractogram (black) for a 16-month-old ferrihydrite sample (0AlFh_Y), the calculated Rietveld refinement derived X-ray diffractogram fit (red), and the difference plot (green).*

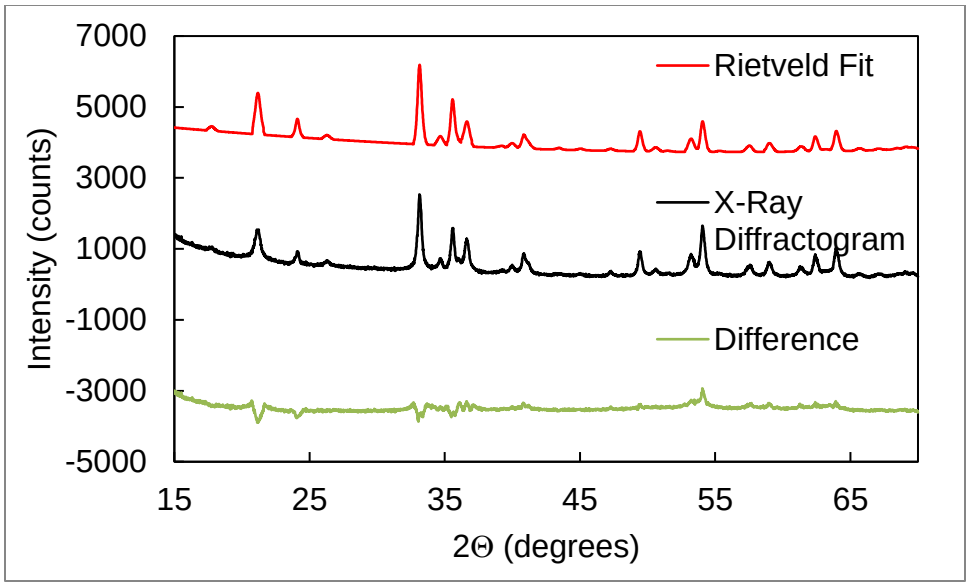

Figure S2.2.4: *Experimental X-ray diffractogram (black) for a 28-month-old ferrihydrite sample (0AlFh_O), the calculated Rietveld refinement derived X-ray diffractogram fit (red) and the difference plot (green).*

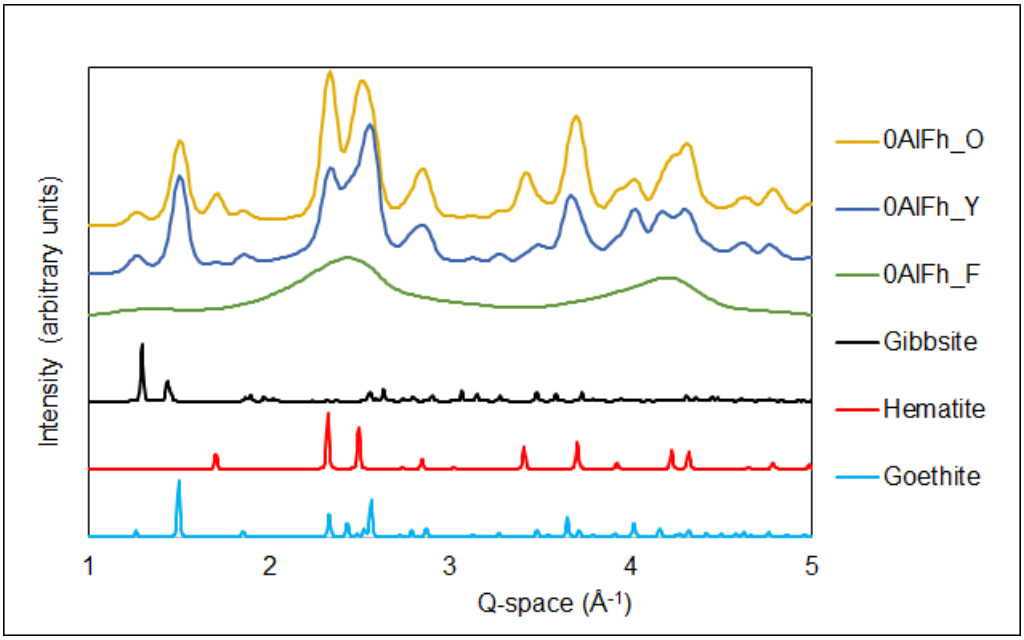

Figure S2.2.5: *Background-removed total scattering, I(Q), for aged pure ferrihydrites with references for gibbsite, hematite, and goethite*

Section S2.3: X-ray magnetic circular dichroism spectra

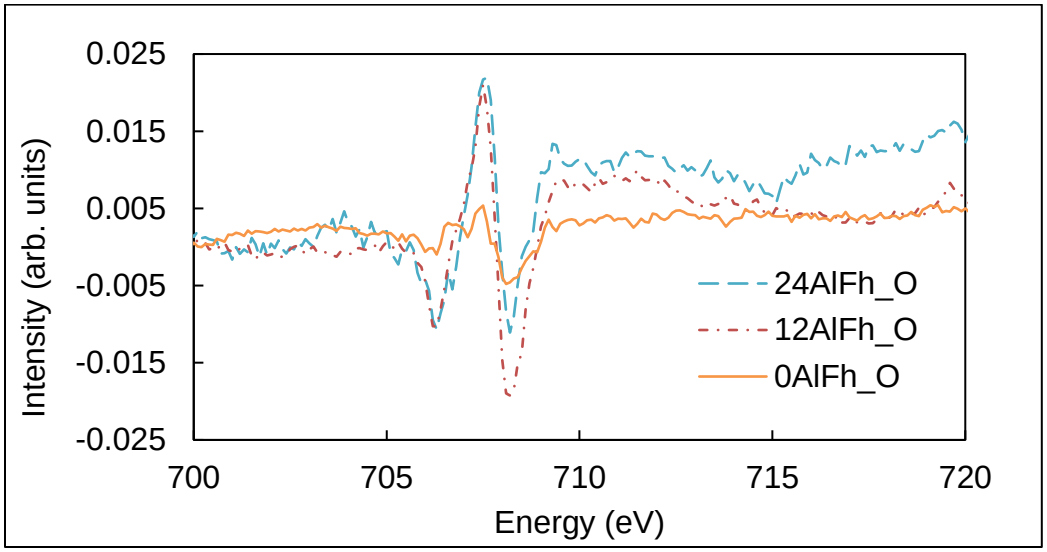

Figure S2.3.1. *Fe L-edge X-ray magnetic circular dichroism spectra of 28-month-old 0AlFh_O, 12AlFh_O, and 24AlFh_O ferrihydrites samples.*

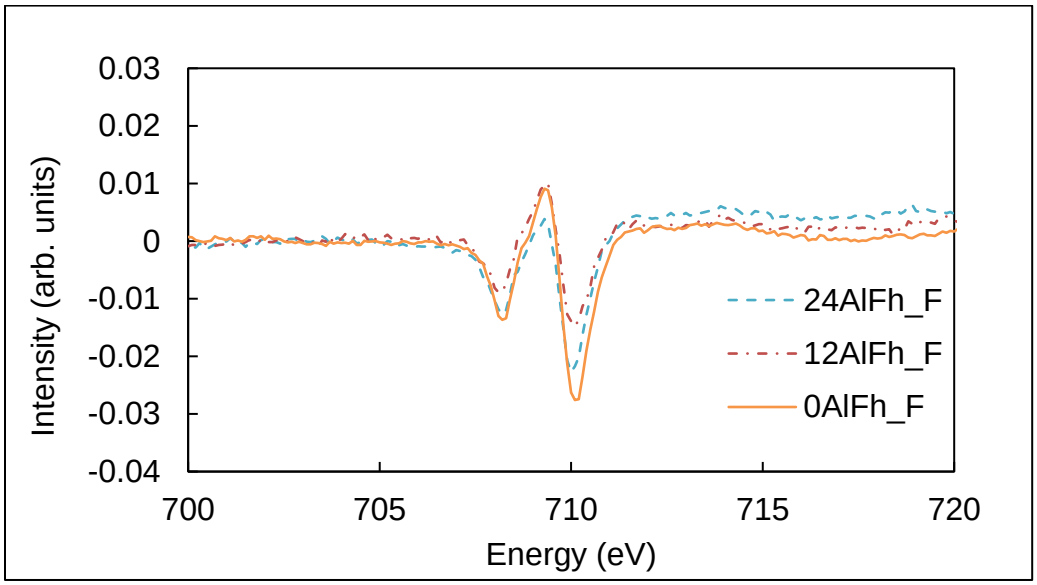

Figure S2.3.2: *Fe L-edge X-ray magnetic circular dichroism spectra of freshly synthesized 0AlFh_F, 12AlFh_F, and 24AlFh_F ferrihydrite samples.*

3 PHOSPHATE ADSORPTION AND CHARACTERIZATION OF AL-BEARING FH

3.1 Introduction

Of the family of ferric iron (Fe(III)) oxides, oxyhydroxides, and hydroxides, Ferrihydrite (Fh; $Fe_5O_8OH.4H_2O$) plays the largest role in regulating the solubility and mobility of anthropogenic pollutants in the environment (Jambor and Dutrizac 1998, Cornell and Schwertmann 2003, Masue et al., 2007, Hochella et al., 2008), mostly because of its large surface areas for which values around 1250 m^2/g have been reported (Villalobos and Antelo 2011). The nanophase nature of Fh and its very small particle size (generally less than 10 nm) had meant that ascertaining its structure has been challenging and subject to an ongoing debate and continued research (Manceau 2019, Sassi and Rosso 2019).

There are two contending models describing the structure of Fh. The Drits model (Drits et al., 1993) for Fh is comprised of three phases, defect-free, defect rich, and hematite-like, all of which consisting of octahedral coordinated Fe. However, this model was challenged by Michel et al. (2007), who put forth a structure that contains both tetrahedrally and octahedrally coordinated Fe. At the core of the debate are questions regarding the presence of tetrahedral Fe(III) and the accounting of defects. Peak and Regier (2012) provided strong corroborating evidence for the presence of tetrahedral Fe based on Fe L-edge X-ray adsorption spectra for Fh compared to other iron oxides with known tetrahedral and octahedral Fe. A recent study used a reverse Monte Carlo approach and demonstrated that only the Michel model could account for the X-ray total scattering data without the need for major fitting (Funnell et al., 2020). Therefore, this study adopts the defect-free Michel model as a starting point for its work.

Elucidating the Fh structure, which until last decade was considered an amorphous enigma, was a significant breakthrough and afforded a solid scaffolding unto which spectroscopic and

computational data join to build mechanistic predictive models (Kabengi et al., 2017, Kubicki et al., 2018, Bompoti et al., 2019). A remaining challenge is to account for the major and minor substituents that are known to get incorporated in the Fh structure and modulate its metastability, crystallinity, evolution, and reactivity. Of these potential dopants, Al remains the most common and possible substitute for Fe in Fh, due to its prevalence and availability within natural systems as well as its similar charge and slightly smaller atomic radius (Shannon 1976). Previous studies on the extent of Al incorporation have shown that the upper limit of Al-doping in Fh is between 20-30% (Cismasu et al., 2012), although Manceau and Gates (2013) refined this value to 25 mol% based on the energetic unfavourability of Al polyhedral being located adjacent to each other. At Al concentrations exceeding approximately 24 mol% (Schwertmann et al., 2000, Cismasu et al., 2012, Manceau and Gates 2013), a distinct aluminous phases, gibbsite (Gb), forms.

In the Michel model, Fe atoms hold three distinct lattice positions designated as Fe_1, Fe_2, and Fe_3: Fe_1 and Fe_2 atoms are octahedrally coordinated to central tetrahedrally coordinated Fe_3 atom (Michel et al., 2007). The Fe_1 sites are the only sites thought to be involved in chemical reactions and bear singly coordinated hydroxyl groups; the Fe_1 sites account for approximately 29% of the total surface according to the existing Fh surface depletion model (Hiemstra 2013). When substitution occurs, the lattice position Al occupies in the structure is not firmly known and is challenging to assess given the limitations of current macroscopic and spectroscopic techniques, particularly at lower Al concentration. Kubicki et al. (2012) used density functional theory calculations and found an energetic preference for Al to substitute for Fe_1 positions. Cismasu et al. (2012) ruled out Al substitution for Fe_3 atoms based on results from X-ray absorption near-edge structure spectroscopy that indicated Al in octahedral coordination, i.e. either in the Fe_1 or Fe_2 position.

Regardless of the lattice position, the incorporation of Al had been shown to influence the sorptive behavior of Fh. For instance, Namayandeh and Kabengi (2019) reported an increase in sulfate sorption, heats of anions exchange, and the ratio of inner-sphere to outer-sphere complexes with increasing Al in synthesized AlFh samples (Namayandeh and Kabengi 2019). Conversely, Johnson and Chrysochoou (2016) observed an increase in the proportion of outer-sphere complexes for selenate, chromate, and sulfate with increasing Al. The adsorption of (oxy)anions, particularly phosphate, on Fe and Al oxides has been studied in the literature (Arai and Sparks 2001, Harvey and Rhue 2008, Antelo et al., 2010, Liu and Hesterberg 2011, Wang et al., 2013, Krumina et al., 2016, Gypser et al., 2018, Liao et al., 2020). Phosphate has been seen to predominantly form inner-sphere binuclear bidentate complexes via ligand exchange with OH^- bearing surface sites or structural water (Wang et al., 2013). In all cases, if ligand exchange and complexation occur predominately on OH-bearing Fe_1 surface sites, then it may be possible to use sorption reactions and accompanying chemical changes, e.g. H^+ release and surface excess, to posit on the location of Al in the Fh structure.

The goal of this work is to posit the location of Al within the existing Fh structural model by characterizing the mineralogy via X-ray diffraction and X-ray total scattering, the surface charge and pH changes via flow microcalorimetric experiments involving phosphate adsorption, and the magnetic properties and atomic coordination geometries via X-ray absorption spectroscopy of freshly synthesized Fh samples with varying Al content. The multi-faceted use of various techniques should help to narrow down the position of Al and provide mechanistic explanations for the macroscopic observations. Ultimately, this understanding can ensure Al is properly parameterized in surface complexation and computational calculations that aim to facilitate the

prediction of the fate and transport of natural and anthropogenic contaminants under environmental conditions.

3.2 Materials and Methods

3.2.1 Sample Synthesis

AlFh samples were freshly synthesized according to a modified version of the Schwertmann and Cornell 2-line Fh protocol (Cornell and Schwertmann 2003). Solutions of 0.2 M $Fe(NO_3)_3$ and 0.2 M $Al(NO_3)_3$ were mixed proportionally to obtain solutions at 0, 12, and 24 mol % Al. The mixed Fe and Al solutions were back titrated to pH values of 7.5 ± 0.1 using a freshly made 1 M KOH solution, centrifuged, and then dialyzed against 18.2 MΩ water until the background conductivity fell below 20 $uS.cm^{-1}$. During each of the three centrifugation steps, the supernatant was preserved, and the concentration of Al in solution determined using an inductively coupled plasma atomic emission spectroscopy (ICP-AES; ARL 3560 ICP analyzer). The synthesized AlFhs samples denoted as 0AlFh, 12AlFh, and 24AlFh for samples containing 0 mol% Al, 12 mol% Al, and 24 mol% Al respectively, were kept in suspensions in sealed containers under aerobic conditions at room temperature until used. At that time, an aliquot was air-dried under the hood for a minimum of 12 hours and ground using a sterile mortar and pestle.

3.2.2 Physical Characterization

A Panalytical XPert Pro X-ray diffractometer was used to obtain X-ray diffraction patterns using CuK-α radiation (45 kV, 40 mA radiation source, 5 – 70˚ 2-theta range, divergence slit size 1˚, step size 0.013˚) and a graphite monochromator to minimize the effects of Fe fluorescence. The software HighScore Plus, by Panalytical (Malvern, United Kingdom), was used for qualitative phase identification. Specific surface area data were obtained using a 7-point Brunauer-Emmett-Teller (BET) method on a Quantachrome AS1Win, Quantachrome Instruments with N_2 gas at a

degassing temperature of 50 ºC for 15 hours. This degassing temperature was selected to mitigate possible secondary phase transformation of the samples.

3.2.3 Total Scattering Analysis

Synchrotron-based X-ray total scattering data were collected on powdered dry 0AlFh samples at beamline 11-ID-B (58.7 keV, λ =0.2113 Å) at the Advanced Photon Source, Argonne National Laboratory. The integration of the raw scattering data into spectra was done using the xPDFsuite, the graphical interface for PDFgetX3 (Juhás et al., 2013). Background intensities were measured directly and subtracted from the sample data to generate I(Q) (i.e., intensity vs. Q-space, where $Q = 4\pi sine\theta/\lambda$). All data regardless of extent of transformation were then normalized based on the chemical composition FeO(OH) to generate the total scattering structure function, S(Q). The S(Q) is then Fourier transformed, using Q_{max} = 25-26 $A^{-1,}$ to generate the PDFs. The PDFs for samples 0AlFh, 12AlFh, and 24AlFh were used as components for ferrihydrite in the pure, 12% Al, and 24% Al series, respectively. The unit cell dimensions for samples were obtained using the software PDFgui by refining a fit to normalized PDFs by varying and fixing several parameters such as scale factor, Q_{damp}, lattice cell parameters, and isotropic thermal parameters.

3.2.4 Magnetic Characterization

X-ray absorption near-edge spectroscopy data were collected at beamline BL6.3.1 at the Advanced Light Source Beamline in Berkeley, CA. Al and O K-edge spectra were collected at room temperature, and Fe L-edge spectra were collected at 20 K. The X-ray absorption spectra were recorded in the total electron yield mode (TEY), and the XMCD spectra were determined by the difference in the x-ray absorption spectra between two oppositely polarized 0.9T magnetic fields. Fe L-edge spectral analysis of Fh provides insight into the coordination geometry of Fe and allows the ratio of tetrahedrally to octahedrally-coordinated Fe(III) ($Fe(III)_{tetra}$:$Fe(III)_{octa}$) to be

estimated. The structural incorporation of Al into Fe_1 sites that are octahedrally-coordinated as we are hypothesizing will increase the values of this ratio.

3.2.5 Phosphate Sorption Experiments and in situ pH measurements

The hypothesis that Al is substituting for the singly coordinated reactive Fe_1 sites on the Fh surface was examined further by conducting phosphate sorption experiments and measuring in-situ changes in pH. Surface complexation occurs only on the singly-coordinated Fe_1 site, with ligand exchange leading to the possible release of H^+ into solution (Hiemstra 2013). The expectation is that, due to the lower thermodynamic stability of the Fe-OH bond (present in Fe_1 polyhedra) compared to that of an Al-OH, less H^+ would be released into solution due to ligand exchange on the surface (Pinney and Morgan 2013). Phosphate sorption experiments were conducted using flow microcalorimeters that were custom fabricated in the Kabengi lab at Georgia State University. The instruments and operating protocols are detailed in previous publications (Rhue et al., 2002, Kabengi et al., 2006, Allen et al., 2017) and are outlined in Section S3.1 of the SI. A known mass (~5.0 mg) of an AlFh sample is packed in the sample holder of the microcalorimeter and flushed with a 0.05 M NaCl solution adjusted to pH 5.6 ± 0.01 until a thermal baseline is obtained. Prior to starting the phosphate experiments, the surface charge was indirectly probed using the energies associated with Cl^- and NO_3^- exchange, Q_{exch}. Due to previously reported similarities in their Q_{exch} magnitude, reaction times, and reversibility, Cl^- and NO_3^- serve as excellent probes of the surface charge (Rhue et al., 2002, Kabengi et al., 2006). To that end, the initial 0.05 M NaCl solution was changed to 0.05 M $NaNO_3$ and the ensuing calorimetric signal associated with NO_3^- replacing Cl^-, [C/N], recorded. Upon completion of the exchange reaction, indicated by the return of the calorimetric signal to the initial thermal baseline, the reverse reaction, i.e., Cl^- replacing NO_3^- or [N/C], is initiated by reverting the solution to 0.05 M NaCl. Repeated

cycles of [C/N] and [N/C] were obtained until the magnitude of Q_{exch} became constant, indicating the surface is equilibrated.

The samples are exposed to phosphate by changing the 0.05 M NaCl solution to one containing 5×10^{-4} M $Na_2H_2PO_4$ and 0.0495 M NaCl at the same pH value of 5.60 ± 0.01. To allow for an even comparison between potentially three different surfaces, the three samples were loaded with the same mass of phosphate, ~ 6.39 µmol. This injection mass was selected based on preliminary results that indicated it would suffice for the reaction to be complete. After the phosphate reaction has ended as indicated by the calorimetric signal return to baseline, [C/N] and [N/C] cycles were performed to immediately probe the phosphated surfaces and ascertain the effect of phosphate adsorption of the reactivity of the surface hydroxyls. During the phosphate experiments and post-phosphate [C/N] and [N/C] cycles, effluents were collected at 5-20 minutes intervals. Phosphate concentrations were measured using an inductively coupled plasma atomic emission spectroscopy (ICP-AES) using an ARL 3560 ICP analyzer. The mass of phosphate adsorbed and subsequently desorbed was calculated as the difference between the mass injected, and that recovered in the effluent. Furthermore, during the adsorption experiments, the pH of the effluent was monitored continuously to investigate the relationship between the adsorption reaction and changes in pH. To that end, the outflow was connected to an in-line flat surface pH probe (Sensorex Model S450; OrionStar A215 pH meter, Fisher Scientific), which sampled pH as a function of time. The probe was calibrated daily using a 3-point calibration.

3.3 Results and Discussion

This work tests the hypothesis that Al atoms that substitute for Fe occupy Fe-OH bearing Fe_1 site in the Michel model, and are thus mostly located on the surface. Replacing all these Fe_1 sites results in an Al concentration that approaches the reported upper limit of substitution, i.e., 24

to 29%. Figure 3-1 shows a model representing a 24AlFh nanoparticle. Replacing all Fe_1 sites with Al would correspond to ~84% of all singly coordinated surface groups being now hydroxyl-bearing Al sites. This incorporation of Al will increase the charge on the surface as the pH_{zpc} of various Al-bearing minerals such as gibbsite has been reported between around 9 to 10, while that of undoped ferrihydrites is around 8 (Hiemstra and Van Riemsdijk 2009, Antelo et al., 2010). This increase has been measured experimentally by Namayandeh and Kabengi (2019).

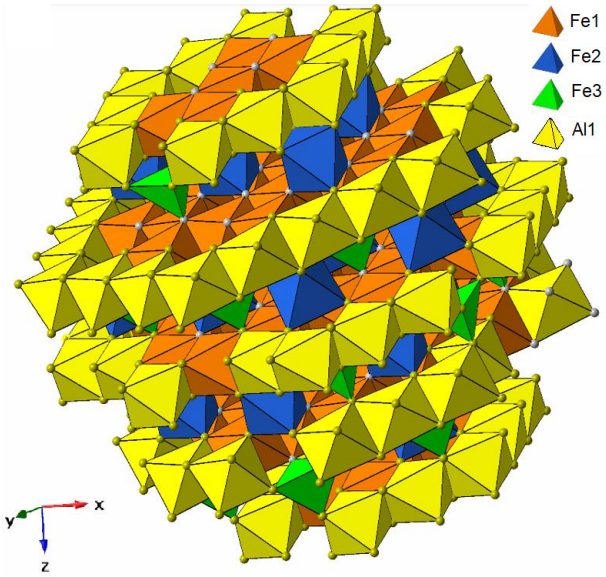

Figure 3-1: Surface depleted 24AlFh nanoparticle with surface Fe1 octahedra replaced with Al with ~ 84% of the surface sites being occupied by Al

3.3.1 Characterization

The summary of the physicochemical properties of the samples is shown in Table 3-1. After synthesis, the concentration of Al in the centrifugation supernatant was measured. Results (Section S3.2 of the SI) show that while the supernatant for 0AlFh and 12AlFh had no detectable Al (instrument detection limit < 10 ppb), we measured 14.44 ± 0.53 ppb of Al in the supernatant recovered from the 24AlFh samples, indicating this sample is nearing the saturation point for Al incorporation.

Table 3-1: The physicochemical properties for freshly synthesized Fh samples with 0, 12 and 24 mol% Al

Sample Name	Surface Area (m^2/g)	Target Al/(Fe+Al) % mol	Measured Al/(Fe+Al) % mol
0AlFh	394	0	0.01 (0.01)[1]
12AlFh	428	12	11.16 (0.01)
24AlFh	516	24	23.31 (0.17)

[1] *Numbers in parentheses correspond to the standard error of the mean.*

Bulk X-ray diffractograms of all samples were consistent with that of 2-line Fh with characteristic peaks occurring at 34 and 61 degrees 2-theta, albeit with slight peak broadening stemming from Al incorporation (Cornell and Schwertmann 2003, Jia et al., 2006) No evidence for any other crystalline Fe, i.e. goethite or hematite, or Al-bearing phases such as Gb (Section S3.3 of the SI) was detected. This finding is to be expected for freshly synthesized samples that had no time to age. Gibbsite only appears in AlFhs with greater than 25 mol% Al (Cismasu et al., 2012, Manceau and Gates 2013).

3.3.2 Microcalorimetry: Pre-Phosphate Injection

Representative raw data (calorimetric signals versus time) for [C/N] and [N/C] exchanges that were obtained on the 0AlFh, 12AlFh and 24AlFh samples are shown in Figure 3-2. For all samples [C/N] was exothermic and [N/C] endothermic, comparable to results from previous microcalorimetric studies on ferrihydrites and other metal oxides (Kabengi et al., 2017, Namayandeh and Kabengi 2019).

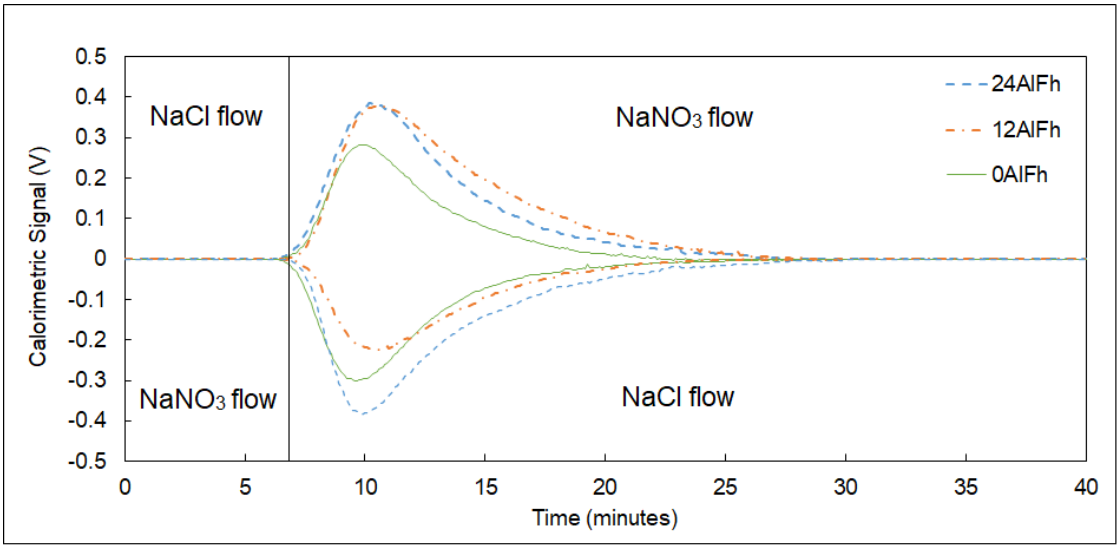

Figure 3-2: Representative calorimetric response for Cl^- and NO_3^- exchanges for 0AlFh, 12AlFh, and 24AlFh. A positive calorimetric peak is indicative of an exothermic reaction, and a negative calorimetric signal is associated with an endothermic reaction.

The mass-normalized Q_{exch} values (mJ/mg) obtained from integrating the calorimetric signals presented in Figure 3-2 are presented in Table 3-2. For each sample, the average magnitude of Q_{exch} associated with [C/N] and [N/C] cycles were similar, indicating the reversibility of the anion exchange reaction. For [C/N], the Q_{exch} was -3.90 ± 0.08 mJ/mg, -3.85 ± 0.11 mJ/mg, and -5.71 ± 0.30 mJ/mg for the 0AlFh, 12AlFh, and 24AlFh samples respectively (Table 3-2). Namayandeh and Kabengi (2019) previously showed a linear increase in Q_{exch} with increasing Al content in AlFh samples with similar Al content and at the same pH value of 5.6. Our results do not seem to distinguish between the 0AlFh and 12AlFh samples that present a significantly smaller Q_{exch} than the 24AlFh sample. The 12AlFh sample is undersaturated with respect to Al content, but by our calculations, the impact of the Al on the surface charge should have been detected. Namayandeh and Kabengi (2019) reported a 0.5 pH unit upward shift in the isoelectric point of the 12AlFh when compared with the 0AlFh. Reasons for this discrepancy are unclear at this time, and further analysis and possible future experiments are needed to elucidate these findings.

Table 3-2: The heat of exchange values (Q_{exch}) for nitrate replacing chloride [C/N] and chloride replacing nitrate [N/C] reactions before phosphate treatment, the Q_{ads} from phosphate treatment, and the amount of adsorbed phosphate for freshly synthesized 0, 12 and 24AlFh samples.

Sample Name	Q_{exch} Pre-Phosphate Treatment (mJ/mg)		Q_{exch} Pre-Phosphate Treatment (mJ/m^2)		Q_{ads} Phosphate (mJ/mg)	Phosphate Adsorbed (µmol/m^2)
	[N/C]	[C/N]	[N/C]	[C/N]		
0AlFh	3.97 (0.14)[1]	-3.90 (0.08)	10.06 (0.35)	-9.91 (0.20)	-14.77	2.71
12AlFh	3.88 (0.09)	-3.85 (0.11)	9.08 (0.21)	-8.99 (0.25)	-15.67	2.63
24AlFh	5.51 (0.17)	-5.71 (0.30)	10.67 (0.33)	-11.08 (0.58)	-16.16	2.1

[1] *Numbers in parentheses correspond to the standard error of the mean*

3.3.3 Microcalorimetry: Phosphate Adsorption

Figure 3-3 shows the heat signals associated with phosphate sorption with the three surfaces. The adsorption of phosphate was exothermic, in line with previously calorimetric results for other oxyanions on metal oxide (Machesky et al., 1989, Malati et al., 1993) and phosphate on mixed Al(III)/Fe(III) systems (Harvey et al., 2008). The peak shapes indicated that phosphate reaction with the AlFhs differed kinetically from Cl/NO_3 exchange in that heat evolved at a much slower rate than Cl/NO_3 exchange, and the reaction lasted considerably longer. In a recent study that integrated calorimetric measurements with time-sequence in situ ATR−FTIR with two-dimensional correlation analysis proposed a two-step mechanism to explain a similar heat signature for phosphate adsorption on lithium cobalt oxide nanoparticle (Laudadio et al., 2019). These steps correspond first to phosphate forming a monodentate complex that upon release of another water molecule transforms into a bidentate deprotonated phosphate coordinated with the surface. We believe a similar mechanism is at play here and explain the slower heat release step observed after 12 to 14 minutes.

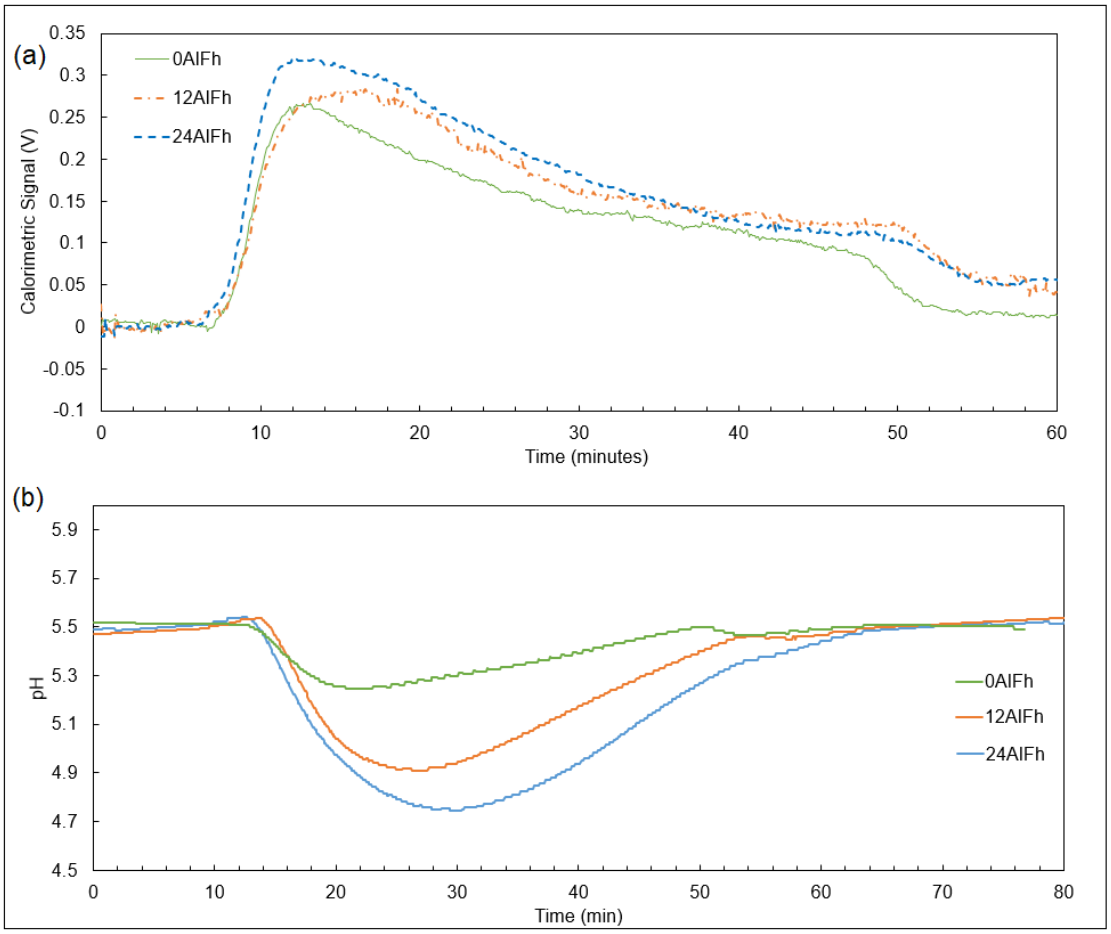

Figure 3-3: (a) Calorimetric signal of phosphate adsorption on a freshly synthesized 0, 12, and 24AlFh samples, (b) pH effects accompanying phosphate adsorption. The experiment was conducted at pH 5.6 ± 0.1, the concentration of phosphate used was 0.0005 M, and the mass of Fh used was ~5mg.

The magnitude of Q_{ads} increased linearly with Al content. This increase is most likely a result of the increased charge as a result of the expected upward shit of the pH_{zpc} stemming from Al substitution. The mass of phosphate retained by each sample was determined by a mass balance calculation between the mass injected (~ 6.39 µmol) and that recovered in all effluents that were collected during phosphate adsorption (Table 3-2). The area-normalized adsorbed masses were calculated at 2.71 µmol/m^2, 2.63 µmol/m^2, and 2.1 µmol/m^2 for the 0AlFh, 12AlFh, and 24AlFh sample respectively. There are two key points to take from these numbers. First, the mass adsorbed in µmol/m^2 are in perfect agreement with those measured by Namayandeh and Kabengi (2019) for

sulfate and by Liao et al., (2020) for phosphate. The values for sulfate sorption were 1.545 μmol/m^2, 2.052 μmol/m^2 and 2.774 μmol/m^2 for 0AlFh, 12AlFh and 24AlFh respectively. Phosphate retained at the surface of lepidocrocite increased from 2.37 μmol/m^2 to 2.91 μmol/m^2. This was attributed to an increase in the proportion of inner-sphere surface complexes due to an increase in available surface site density (Liao et al., 2020). Second, unlike the aforementioned studies, there was no positive linear relationship between phosphate adsorbed and Al content in our samples. The 12AlFh and 24AlFh samples had markedly higher SSA than those synthesized by Namayandeh and Kabengi (2019) mostly due to the lower degassing temperature that was chosen. Furthermore, our choice to inject a fixed mass of phosphate on all three surfaces may have overlooked that the tallied masses may occur at different points of the reaction equilibrium and leave an uneven portion of sites unoccupied. The mass chosen was based on an estimation of full coverage from preliminary experiments, but small errors may have compromised obtaining an accurate trend.

During the phosphate adsorption experiments, pH measurements were taken concurrently with the microcalorimetric measurements, and these measurements are plotted as a function of time (Figure 3-3.3b). Although all solutions used for the adsorption experiments were pH adjusted to 5.6 ± 0.1, the pH response (Figure 3-3.3b) did not entirely return to the original pre-treatment pH values after 80 minutes. The baseline shifts were mathematically corrected. As stated above, we suspect the phosphate reaction to encompass two steps, with the second step being kinetically slower than the first. This could mean that the release of H^+, identified by a drop in pH, accompanying the reactions is delayed and may not have been adequately captured at the time, as we interrupted the flow of the phosphate solution and returned to the NaCl solution.

Qualitatively, we can assess that there is more pH decrease with increasing Al content. We hypothesize that owing to its higher pKa, an Al-OH would deprotonate less readily at a given pH value, and this is reflected in the mass of protons obtained for the 0AlFh and 24AlFh. However, the opposite is seen in the results which may be indicative of another underlying process leading to the release of H^+ which would lead to a sharper pH drop.

3.3.4 Spectroscopic Analysis

3.3.4.1 X-Ray circular dichroism spectroscopy

Figure 3-4 shows the XMCD spectra along with an annotation of each Fe component that contributes to the overall signal. Although all three samples possess a magnetic moment and spectral contributions from octahedral Fe(II), tetrahedral Fe(III), and octahedral Fe(III), there were notable differences in magnitude and intensities across samples. First, the undoped 0AlFh sample has a larger magnetic moment based on spectral peak intensities. Second, an increase in Al is accompanied by an increase in the $Fe(III)_{tetra}$:$Fe(III)_{octa}$ ratio. A study (Guyodo et al., 2012) varied the $Fe(III)_{tetra}$:$Fe(III)_{octa}$ ratios and examined the resulting simulated XMCD spectra. They observe similar changes and spectra (Fe component peak locations and shift of intensities) to those reported in this study, further corroborating our conclusion that increasing Al does increase the $Fe(III)_{tetra}$:$Fe(III)_{octa}$ ratios. Both these observations suggest that in concurrence with Cismasu et al., (2012), Al is replacing an octahedrally-coordinated site, either Fe_1 or Fe_2. The established surface depletion model of Fh is depleted with respect to Fe_2 and Fe_3 (Hiemstra 2013). Thus, if one constrains Al substitution to the surface, it is most likely that it is the octahedral Fe_1 sites that are being substituted for Al.

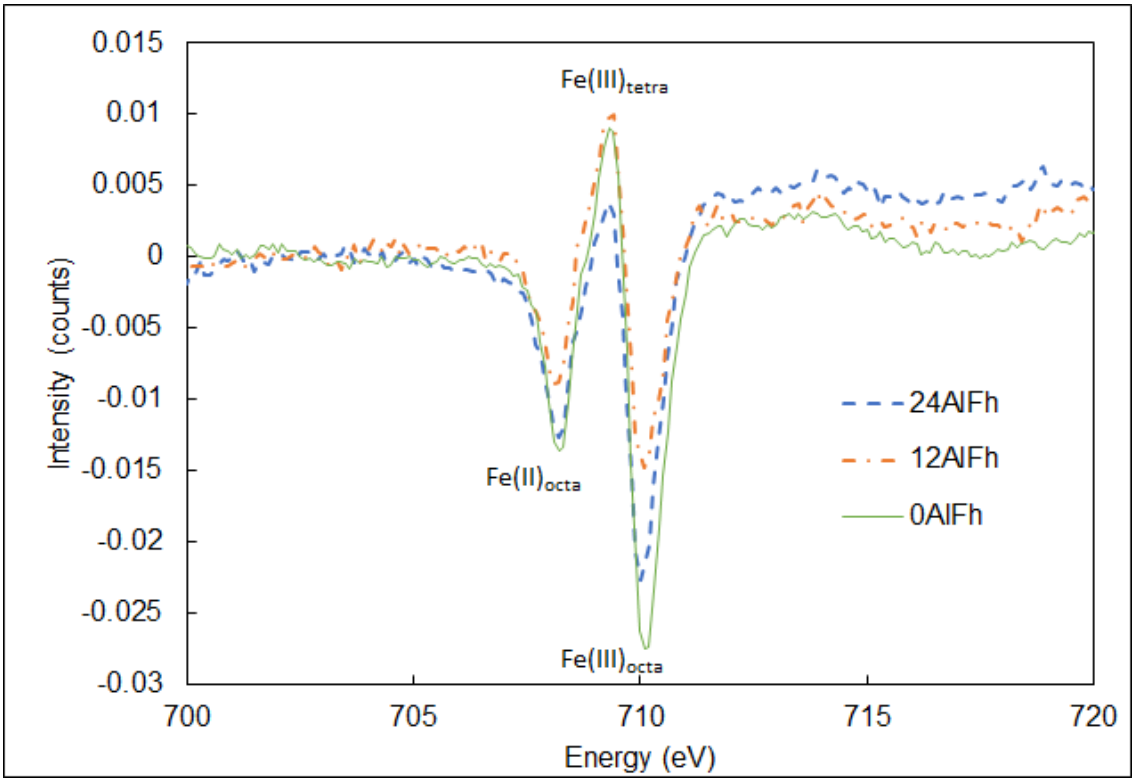

Figure 3-4: X-ray magnetic circular dichroic spectra of a 0, 12, and 24AlFh showing the component contributions of octahedral Fe(II), tetrahedral Fe(III) and octahedral Fe(III) to the spectra

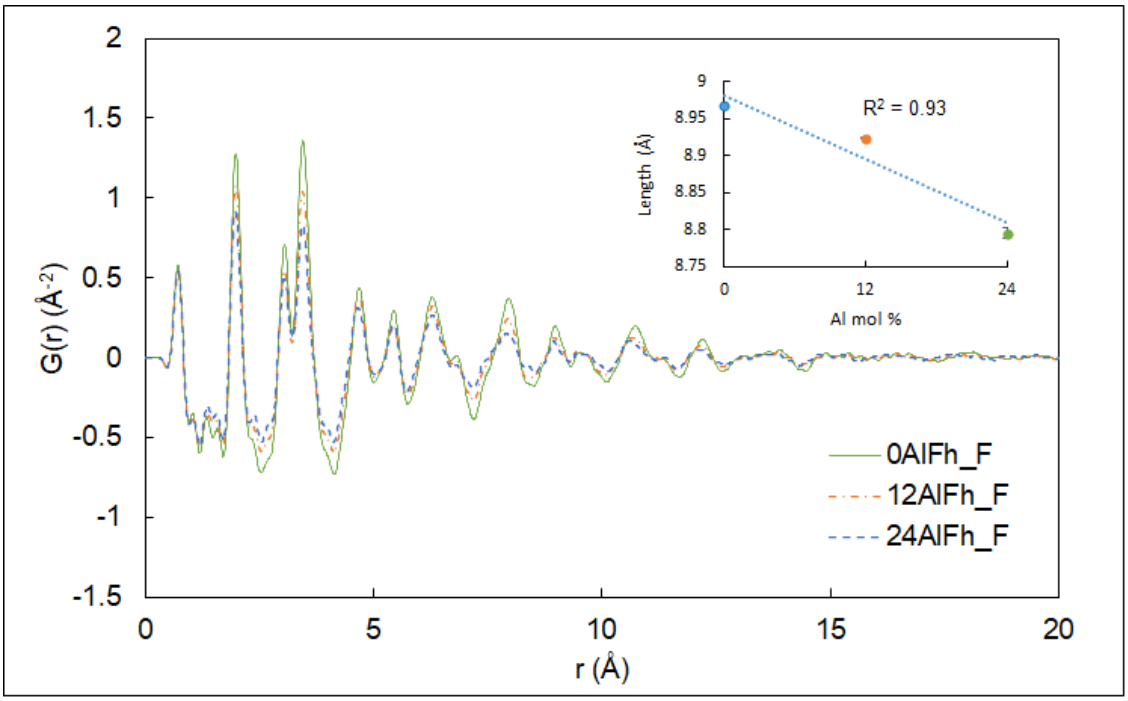

Figure 3-5: (a) Overlaid experimental PDF plots for 0, 12 and 24AlFh samples; (inset) plot showing a linear decrease of the C-axis unit cell parameters derived from the fitting of the experimental data with increasing Al mol%

PDFs obtained on 0, 12, and 24AlFh were similar to previously reported X-ray total scattering spectra for ferrihydrites and lepidocrocite (Figure 3-5). There was a decrease in the PDF intensities and spectral attenuation at higher radial distances with increasing mol% Al (Michel et al., 2007, Michel et al., 2010, Cismasu et al., 2012, Liao et al., 2020). The PDF fitting was performed initially using a pure Fh structure, which was then parameterized and refined to obtain unit cell lattice parameters. The refined 0AlFh structure was used as the initial basis or starting point for the subsequent 12AlFh and 24AlFh refinements.

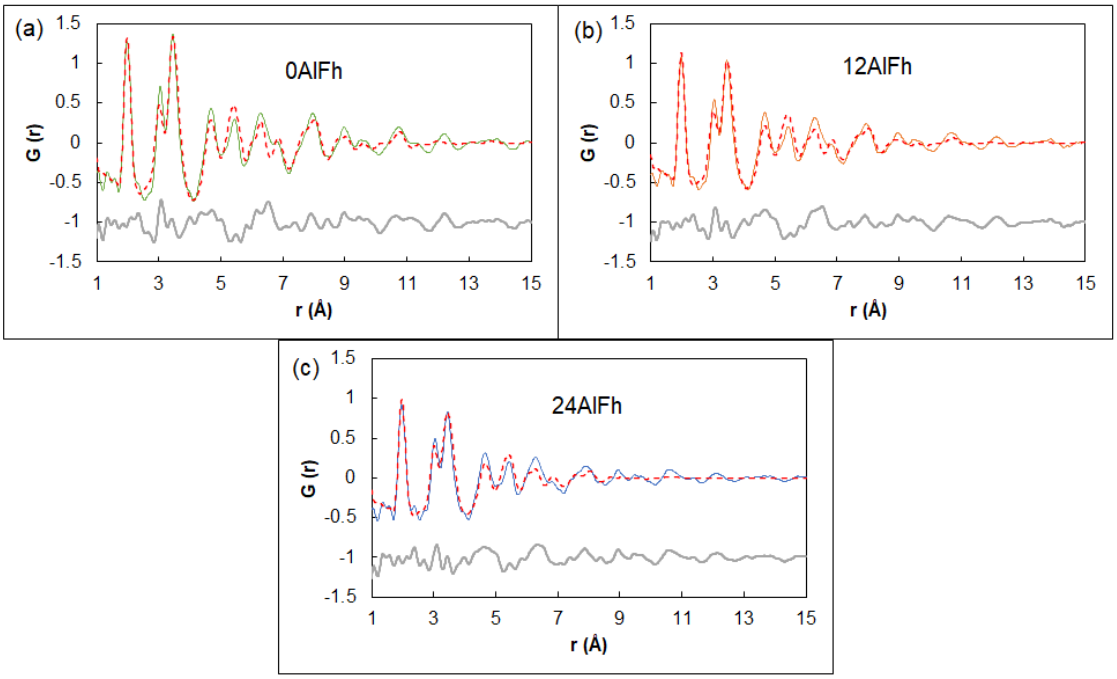

Figure 3-6: Experimental PDF (solid lines) plotted against the calculated PDF fit (dashed red lines) derived from a parameterized Fh structural model for an (a)0AlFh (green), (b) 12AlFh (orange), (c) and 24AlFh (blue). Difference plots between calculated and experimental data are shown in grey.

Figure 3-6 shows the experimental PDF datasets overlaid with their respective parameterized fits. The weighted profile R-factor, R_{wp}, were 0.28, 0.20, and 0.31 for 0AlFh, 12AlFh, and 24AlFh respectively and slightly larger than what is typically expected from Rietveld-like refinements ($R_{wp} < 0.10$). The larger R_{wp} is likely due to some peaks not being sufficiently resolved within the experimental data. The increasing R_{wp} with increasing Al is most likely due to Al atoms not being incorporated into the theoretical model as would be necessary to accurately assess the effects of the slightly smaller atomic radii of Al compared to Fe (0.54 to 0.65 Å, respectively (Shannon 1976)) on these PDF-derived lattice parameters. The lattice parameters that were derived from these fits showed a linear decrease in the c-axis with increasing Al (Figure 3-5 inset), which is also consistent with previous studies. Al incorporation has been shown to decrease

radial distances between edge-sharing octahedra as well as that of corner-sharing octahedra (Michel et al., 2007, Cismasu et al., 2012).

3.4 Significance and Conclusion

This work utilized flow microcalorimetry, and various X-ray spectroscopic techniques in an attempt to ascertain the position of Al when it substitutes into the Fe site. Specifically, we hypothesized that Al replaces an octahedrally-coordinated Fe_1 site on the surface and had intended to rely primarily on pH changes that accompany ligand adsorption to test this hypothesis. Taken together, the bulk of data collected during this study seems to indicate the presence of Al in either one of the octahedral Fe positions. Some unanticipated sorption trends and the difficulty in decoupling the surface charge effect from pH data did not allow us to rule on our hypothesis conclusively. However, further refinement of fits, especially those of the PDF X-ray total scattering data, would allow for more precision in ascertaining the location of Al within the Fh structure. XMCD provided initial evidence for a decrease in the ratio of octahedrally coordinated Fe(III) relative to that of tetrahedrally coordinated Fe(III). Further critical analysis by quantification of Fe component distributions in the XMCD spectra of AlFhs may help to solidify the argument that Al is occupying surface Fe_1 octahedra, with the ultimate aim of shedding light on the true position of Al within the structure. Seldom is Fh found in environmental systems without impurities and this highlights the need for theoretical models that can account for the effects of Al, but in order to do so, the location of Al in Fh must be better understood.

3.5 Acknowledgments

I would like to acknowledge Dr. Marc Michel for helping obtain and interpret X-ray total scattering data as well as Dr. Kevin Rosso and Dr. Carolyn Pearce for helping to obtain and interpret the XAS and XMCD data. I would like to acknowledge Dr. Daniel Gebregiorgis for his

help with the collection of powder XRD data. I would also like to acknowledge Brianne Martin and Gabrial Goldner for their work on the microcalorimetric data collection. I would like to acknowledge Dr. Tjisse Hiemstra for the use of his surface depletion Fh CrystalMaker file.

REFERENCES

Allen, N., M. L. Machesky, D. J. Wesolowski, N. J. J. o. c. Kabengi and i. science (2017). "Calorimetric study of alkali and alkaline-earth cation adsorption and exchange at the quartz-solution interface." **504**: 538-548.

Antelo, J., S. Fiol, C. Perez, S. Marino, F. Arce, D. Gondar and R. Lopez (2010). "Analysis of phosphate adsorption onto ferrihydrite using the CD-MUSIC model." J Colloid Interface Sci **347**(1): 112-119.

Arai, Y. and D. L. Sparks (2001). "ATR–FTIR Spectroscopic Investigation on Phosphate Adsorption Mechanisms at the Ferrihydrite–Water Interface." Journal of Colloid and Interface Science **241**(2): 317-326.

Bompoti, N. M., M. Chrysochoou, M. L. J. E. s. Machesky and technology (2019). "A unified surface complexation modeling approach for chromate adsorption on iron oxides." **53**(11): 6352-6361.

Cismasu, A. C., F. M. Michel, J. F. Stebbins, C. Levard and G. E. Brown (2012). "Properties of impurity-bearing ferrihydrite I. Effects of Al content and precipitation rate on the structure of 2-line ferrihydrite." Geochimica et Cosmochimica Acta **92**: 275-291.

Cismasu, A. C., F. M. Michel, J. F. Stebbins, C. Levard and G. E. J. G. e. C. A. Brown Jr (2012). "Properties of impurity-bearing ferrihydrite I. Effects of Al content and precipitation rate on the structure of 2-line ferrihydrite." **92**: 275-291.

Cornell, R. M. and U. Schwertmann (2003). The iron oxides: structure, properties, reactions, occurrences and uses, John Wiley & Sons.

Drits, V., B. Sakharov, A. Salyn and A. Manceau (1993). "Structural model for ferrihydrite." Clay Minerals **28**(2): 185-207.

Funnell, N. P., M. F. Fulford, S. Inoué, K. Kletetschka, F. M. Michel and A. L. J. C. C. Goodwin (2020). "Nanocomposite structure of two-line ferrihydrite powder from total scattering." **3**(1): 1-9.

Guyodo, Y., P. Sainctavit, M. A. Arrio, C. Carvallo, R. L. Penn, J. J. Erbs, B. S. Forsberg, G. Morin, F. Maillot and F. J. G. Lagroix, Geophysics, Geosystems (2012). "X-ray magnetic circular dichroïsm provides strong evidence for tetrahedral iron in ferrihydrite." **13**(6).

Gypser, S., F. Hirsch, A. M. Schleicher and D. Freese (2018). "Impact of crystalline and amorphous iron- and aluminum hydroxides on mechanisms of phosphate adsorption and desorption." Journal of Environmental Sciences **70**: 175-189.

Harvey, O. R. and R. D. Rhue (2008). "Kinetics and energetics of phosphate sorption in a multi-component Al(III)–Fe(III) hydr(oxide) sorbent system." Journal of Colloid and Interface Science **322**(2): 384-393.

Hiemstra, T. (2013). "Surface and mineral structure of ferrihydrite." Geochimica et Cosmochimica Acta **105**: 316-325.

Hiemstra, T. and W. H. Van Riemsdijk (2009). "A surface structural model for ferrihydrite I: Sites related to primary charge, molar mass, and mass density." Geochimica et Cosmochimica Acta **73**(15): 4423-4436.

Hochella, M. F., S. K. Lower, P. A. Maurice, R. L. Penn, N. Sahai, D. L. Sparks and B. S. J. s. Twining (2008). "Nanominerals, mineral nanoparticles, and earth systems." **319**(5870): 1631-1635.

Jambor, J. L. and J. E. Dutrizac (1998). "Occurrence and Constitution of Natural and Synthetic Ferrihydrite, a Widespread Iron Oxyhydroxide." Chemical Reviews **98**(7): 2549-2586.

Jia, Y., L. Xu, Z. Fang, G. P. J. E. s. Demopoulos and technology (2006). "Observation of surface precipitation of arsenate on ferrihydrite." **40**(10): 3248-3253.

Juhás, P., T. Davis, C. L. Farrow and S. J. J. J. o. A. C. Billinge (2013). "PDFgetX3: a rapid and highly automatable program for processing powder diffraction data into total scattering pair distribution functions." **46**(2): 560-566.

Kabengi, N. J., M. Chrysochoou, N. Bompoti and J. D. Kubicki (2017). "An integrated flow microcalorimetry, infrared spectroscopy and density functional theory approach to the study of chromate complexation on hematite and ferrihdyrite." Chemical Geology **464**: 23-33.

Kabengi, N. J., R. D. Rhue and S. H. Daroub (2006). "Using flow calorimetry to determine the molar heats of cation and anion exchange and the point of zero net charge on amorphous aluminum hydroxides." Soil science **171**(1): 13-20.

Kabengi, N. J., R. D. Rhue and S. H. J. S. s. Daroub (2006). "Using flow calorimetry to determine the molar heats of cation and anion exchange and the point of zero net charge on amorphous aluminum hydroxides." **171**(1): 13-20.

Krumina, L., J. P. L. Kenney, J. S. Loring and P. Persson (2016). "Desorption mechanisms of phosphate from ferrihydrite and goethite surfaces." Chemical Geology **427**: 54-64.

Kubicki, J. D., N. Kabengi, M. Chrysochoou and N. J. G. t. Bompoti (2018). "Density functional theory modeling of chromate adsorption onto ferrihydrite nanoparticles." **19**(1): 8.

Laudadio, E. D., P. Ilani-Kashkouli, C. M. Green, N. J. Kabengi and R. J. J. L. Hamers (2019). "Interaction of phosphate with lithium cobalt oxide nanoparticles: a combined spectroscopic and calorimetric study." **35**(50): 16640-16649.

Liao, S., X. Wang, H. Yin, J. E. Post, Y. Yan, W. Tan, Q. Huang, F. Liu and X. Feng (2020). "Effects of Al substitution on local structure and morphology of lepidocrocite and its phosphate adsorption kinetics." Geochimica et Cosmochimica Acta.

Liu, Y. T. and D. Hesterberg (2011). "Phosphate bonding on noncrystalline Al/Fe-hydroxide coprecipitates." Environ Sci Technol **45**(15): 6283-6289.

Machesky, M. L., B. L. Bischoff, M. A. J. E. s. Anderson and technology (1989). "Calorimetric investigation of anion adsorption onto goethite." **23**(5): 580-587.

Malati, M. A., R. A. Fassam, I. R. J. J. o. C. T. Henderson and Biotechnology (1993). "Mechanism of phosphate interaction with two reference clays and an anatase pigment." **58**(4): 387-389.

Manceau, A. (2019). "Comment on “Roles of Hydration and Magnetism on the Structure of Ferrihydrite from First Principles”." ACS Earth and Space Chemistry **3**(8): 1576-1580.

Manceau, A. and W. P. Gates (2013). "Incorporation of Al in iron oxyhydroxides: implications for the structure of ferrihydrite." Clay Minerals **48**(3): 481-489.

Masue, Y., R. H. Loeppert and T. A. Kramer (2007). "Arsenate and Arsenite Adsorption and Desorption Behavior on Coprecipitated Aluminum:Iron Hydroxides." Environmental Science & Technology **41**(3): 837-842.

Michel, F. M., V. Barron, J. Torrent, M. P. Morales, C. J. Serna, J. F. Boily, Q. Liu, A. Ambrosini, A. C. Cismasu and G. E. Brown, Jr. (2010). "Ordered ferrimagnetic form of ferrihydrite reveals links among structure, composition, and magnetism." Proc Natl Acad Sci U S A **107**(7): 2787-2792.

Michel, F. M., L. Ehm, S. M. Antao, P. L. Lee, P. J. Chupas, G. Liu, D. R. Strongin, M. A. Schoonen, B. L. Phillips and J. B. J. S. Parise (2007). "The structure of ferrihydrite, a nanocrystalline material." **316**(5832): 1726-1729.

Michel, F. M., L. Ehm, S. M. Antao, P. L. Lee, P. J. Chupas, G. Liu, D. R. Strongin, M. A. A. Schoonen, B. L. Phillips and J. B. Parise (2007). "The Structure of Ferrihydrite, a Nanocrystalline Material." Science **316**(5832): 1726-1729.

Namayandeh, A. and N. Kabengi (2019). "Calorimetric study of the influence of aluminum substitution in ferrihydrite on sulfate adsorption and reversibility." J Colloid Interface Sci **540**: 20-29.

Pinney, N. and D. Morgan (2013). "Thermodynamics of Al-substitution in Fe-oxyhydroxides." Geochimica et Cosmochimica Acta **120**: 514-530.

Rhue, R., C. Appel and N. J. S. s. Kabengi (2002). "Measuring surface chemical properties of soil using flow calorimetry 1." **167**(12): 782-790.

Sassi, M. and K. M. Rosso (2019). "Reply to “Comment on ‘Roles of Hydration and Magnetism on the Structure of Ferrihydrite from First Principles’”." ACS Earth and Space Chemistry **3**(8): 1581-1583.

Schwertmann, U., J. Friedl, H. Stanjek and D. G. Schulze (2000). "The effect of Al on Fe oxides. XIX. Formation of Al-substituted hematite from ferrihydrite at 25 C and pH 4 to 7." Clays and Clay Minerals **48**(2): 159-172.

Shannon, R. D. (1976). "Revised effective ionic radii and systematic studies of interatomic distances in halides and chalcogenides." Acta crystallographica section A: crystal physics, diffraction, theoretical and general crystallography **32**(5): 751-767.

Villalobos, M. and J. J. R. i. d. c. a. Antelo (2011). "A unified surface structural model for ferrihydrite: Proton charge, electrolyte binding, and arsenate adsorption." **27**(2): 139-151.

Wang, X., W. Li, R. Harrington, F. Liu, J. B. Parise, X. Feng and D. L. Sparks (2013). "Effect of ferrihydrite crystallite size on phosphate adsorption reactivity." Environmental science & technology **47**(18): 10322-10331.

SUPPLEMENTARY INFORMATION FOR CHAPTER 3

Section S3.1: Instrumentation and basic operational procedure for the flow microcalorimeter

The flow microcalorimeter consists of a glass microcolumn apparatus with a sample holder into which a known mass of the sample is packed. A solution containing the chemical species of interest is flushed through the packed microcolumn at a controlled flow rate, which is continuously monitored and adjusted as needed to remain constant between 0.30 to 0.330 ml min^{-1}), until the thermal equilibrium is obtained as evidenced by a steady calorimetric baseline. The input solution is switched to another solution of a different composition e.g., pH, ionic strength, or concentration, and the change in the solution temperature resulting from either heat produced or consumed as the solute interacts with the solid is monitored. A pair of thermistors, one upstream and one downstream from the sample holder, form one half of an electronic bridge that senses the temperature of the solution and generates an electrical signal. This calorimetric signal is displayed graphically and recorded as a function of time. The end of the reactions is observed when the calorimetric signal return to the initial thermal baseline. The peak areas are obtained by integrating the calorimetric peak relative to flow rate. The heats of reactions (Q in mJ/mg of packed solid) are calculated by converting the peak areas to energy units (J) using peaks of known energy input generated from a calibrating resistor located in the flow stream near the microsample holder. Figure S3.1.1 shows a series of heat pulses and the associated calibration curve.

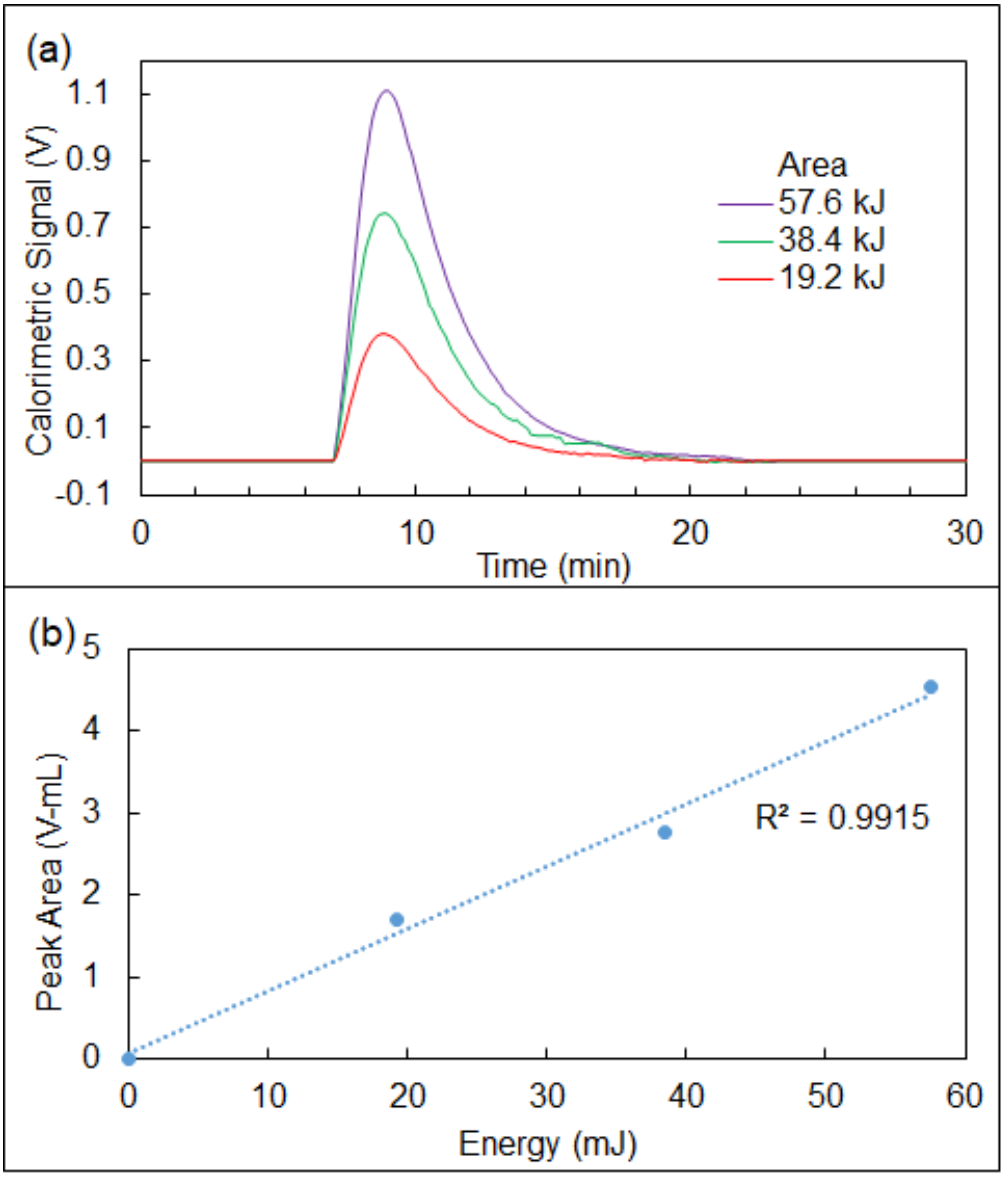

Figure S3.1.1: *Peaks obtained from a series of times heat pulses (top) and the corresponding calibration curves (bottom).*

Section S3.2: Aluminum concentrations in the supernatant

Table 3.2.1: *The measured concentrations of Al found in the supernatant of freshly synthesized 0, 12 and 24 mol% ferrihydrites. (Note: N/A is indicative of concentrations of Al being under the instrument detection limit < 0.01 ppm)*

Sample Name	Target Al mol %	Sample Description	Al_1 (ppm)	Al_2 (ppm)	Al_3 (ppm)	Average Al (ppm)	Average Al (ppb)
Sample 1	0	0Al_1_1st	N/A	N/A	N/A	N/A	N/A
Sample 2	0	0Al_4_1st	N/A	N/A	N/A	N/A	N/A
Sample 3	0	0Al_5_1st	N/A	N/A	N/A	N/A	N/A
Sample 4	0	0Al_1_2nd	N/A	N/A	N/A	N/A	N/A
Sample 5	0	0Al_4_2nd	0.015	0.015	0.016	0.015	15.333
Sample 6	0	0Al_5_2nd	N/A	N/A	N/A	N/A	N/A
Sample Name	Target Al mol %	Sample Description	Al_1 (ppm)	Al_2 (ppm)	Al_3 (ppm)	Average Al (ppm)	Average Al (ppb)
Sample 7	12	12Al_2_1st	N/A	N/A	N/A	N/A	N/A
Sample 8	12	12Al_3_1st	N/A	N/A	N/A	N/A	N/A
Sample 9	12	12Al_5_1st	N/A	N/A	N/A	N/A	N/A
Sample 10	12	12Al_2_2nd	N/A	N/A	N/A	N/A	N/A
Sample 11	12	12Al_3_2nd	N/A	N/A	N/A	N/A	N/A
Sample 12	12	12Al_5_2nd	N/A	N/A	N/A	N/A	N/A
Sample Name	Target Al mol %	Sample Description	Al_1 (ppm)	Al_2 (ppm)	Al_3 (ppm)	Average Al (ppm)	Average Al (ppb)
Sample 13	24	24Al_1_1st	0.015	0.016	0.016	0.016	15.667
Sample 14	24	24Al_2_1st	0.015	0.013	0.015	0.014	14.333
Sample 15	24	24Al_3_1st	0.015	0.015	0.015	0.015	15.000
Sample 16	24	24Al_1_2nd	0.014	0.014	0.015	0.014	14.333
Sample 17	24	24Al_2_2nd	0.014	0.016	0.016	0.015	15.333
Sample 18	24	24Al_3_2nd	0.011	0.013	0.012	0.012	12.000

Section S3.3: X-ray diffractograms

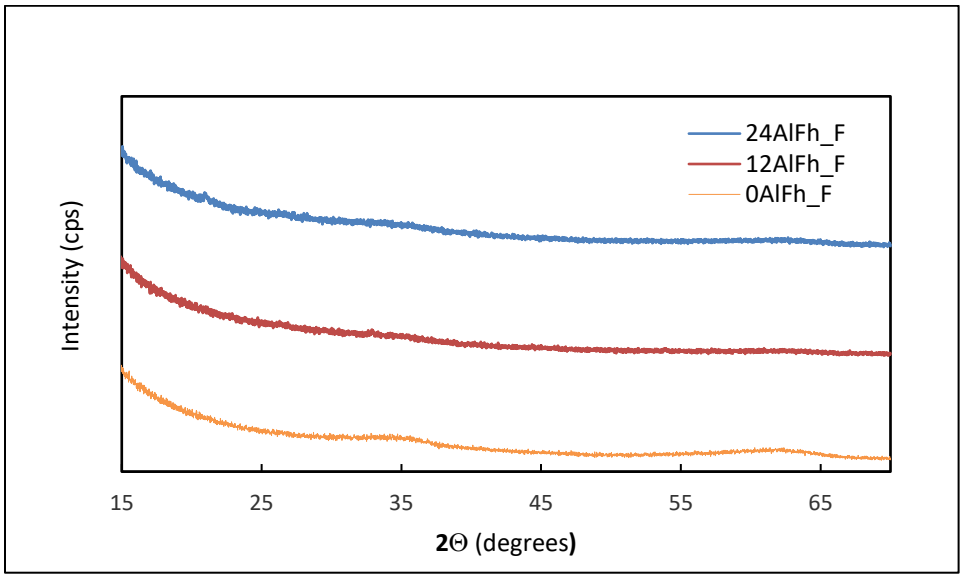

Figure S3.3.1: *X-ray diffractogram of freshly synthesized ferrihydrites with 0, 12, and 24 mol % Al.*

4 CONCLUSIONS

This thesis examined the mechanisms by which Fh and AlFh transform in secondary crystalline products under environmentally relevant conditions, the nature of anion exchange and ligand sorption interactions on aged Fh and AlFh, and the location of Al in the structure of Fh based on the characterization of freshly synthesized AlFhs.

In Chapter 2, one of the key findings was the significant impact of aging, particularly on undoped Fh. Aged Fh clearly showed evidence of an increasing extent of phase transformation with age, which resulted in lower Q_{exch}, decreased surface area, and increases in the ratio of hematite (Ht) to goethite (Gt). Based on X-ray diffraction peaks, however, it may be inferred that Ht, at these particular conditions, forms directly from Fh and not Gt, as some studies have suggested. These findings on the pure Fh, however, are not a complete depiction of what happens to Fh, particularly in the environment. Al incorporation is prevalent in naturally occurring Fhs and almost seldom does one find a pure Fh in environmental systems. AlFh may be active in these systems over long durations of time and may be exposed to a wide range of environmental conditions. This study shows that Al prevents transformation of Fh, and Al incorporation prevents the observed decrease in surface seen in pure Fh with aging and appears to stabilize the magnetic properties of AlFh.

In Chapter 3, spectroscopic techniques such as X-ray diffraction, X-ray magnetic circular dichroism spectroscopy (XMCD), coupled with thermodynamic data derived from flow microcalorimetry, were used to ascertain the location of Al within the Fh structure based on the Michel model. XMCD spectroscopic analyses did show evidence to help corroborate the first hurdle needed to answer this question. Al in AlFh has been found to be octahedrally coordinated based on X-ray absorption spectroscopy. This finding at least definitively points towards Al

occupation occurring in either the symmetry-designated Fe_1 and/or Fe_2 octahedral position. Fe_1 are the dominant reactive surface sites and thus, probing anion interactions with the surface was conducted in an attempt to discern between a Fe_1 or an Al_1 surface site. We see an increase in the heats of exchange, Q_{exch}, for phosphate with increasing mol% Al which is consistent with previous studies. The increased pH drop with increasing Al may also be explanatory for surface complexation behavior with more H^+ being released due to more deprotonated bidentate inner-sphere complexation occurring. However, analysis of the mass of phosphate adsorbed on the surface was inconclusive compared to other studies on phosphate adsorption on iron oxides; the changes in the amount of phosphate adsorbed could be due to the effect of Al incorporation on reactive site densities however further systematic work would be needed to evidence to prove the existence of Al_1 substitution.

Overall, this work served to answer two main questions: what the influences of Al and aging on Fh are and can the position of isostructural-substituted Al be determined. In answering the first question, we determine that the presence of Al inhibits the phase transformation induced by aging. This effect, we posit, is responsible for the persistence of Fhs in nature much longer than one expects based on bench observations. Looking forward, a continuation of the long-term characterization will help refine the combined impact, namely on elucidating the direction of secondary transformations. The answer to the latter question remains elusive, albeit with narrowed possibilities. In positioning the Al on the surface in an octahedrally-coordinated Fe site, one out of the three possible positions has all but been ruled out. The characterization of Fh, particularly structurally is challenging. Moreover, it is worthwhile to keep in mind that models for Fhs are idealized and may not always be possible to reconcile them with the reality of Fh nature. In all cases, this work demonstrates the strength of coupling of a wide range of analytical techniques.

Integrating their results is an ideally systematic way to characterize Fh properties that would otherwise remain inaccessible.